DIGITAL ACCESS TO
SCHOLARSHIP AT HARVARD
DASH.HARVARD.EDU

HARVARD LIBRARY
Office for Scholarly Communication

Superconducting Coplanar Waveguides for High Fidelity Operation of Quantum Repeaters

Citation

Williams, Conner. 2021. Superconducting Coplanar Waveguides for High Fidelity Operation of Quantum Repeaters. Bachelor's thesis, Harvard College.

Permanent link

https://nrs.harvard.edu/URN-3:HUL.INSTREPOS:37368577

Terms of Use

This article was downloaded from Harvard University's DASH repository, and is made available under the terms and conditions applicable to Other Posted Material, as set forth at http://nrs.harvard.edu/urn-3:HUL.InstRepos:dash.current.terms-of-use#LAA

Share Your Story

The Harvard community has made this article openly available.
Please share how this access benefits you. Submit a story .

Accessibility

Superconducting Coplanar Waveguides for High Fidelity Operation of Quantum Repeaters

by

Conner Williams

Submitted to the Departments of Physics and Computer Science
in partial fulfillment of the requirements for the degree of

Joint Bachelor of Arts in Physics and Computer Science

at

HARVARD UNIVERSITY

May 2021

Author . . . .
Conner Williams
Departments of Physics and Computer Science
March 26, 2021

Certified by . . . .
Mikhail Lukin
George Vasmer Leverett Professor of Physics
Thesis Supervisor

Superconducting Coplanar Waveguides for High Fidelity Operation of Quantum Repeaters

by

Conner Williams

Submitted to the Departments of Physics and Computer Science
on March 26, 2021, in partial fulfillment of the
requirements for the degree of
Joint Bachelor of Arts in Physics and Computer Science

Abstract

Quantum repeaters, and the quantum communication they enable, are as vital to the efficient use of quantum computers as the internet is to current computing. The Lukin Group has developed a repeater architecture using Silicon Vacancy Centers in diamond, and members have used it to experimentally demonstrate single-qubit communication. Currently, though, its circuit depth and two-qubit functionality are limited by heating due to microwave driving from gold coplanar waveguides (CPW) atop the diamond's surface. To break through this barrier, superconducting CPW's, which do not dissipate heat, have been developed.

Thesis Supervisor: Mikhail Lukin
Title: George Vasmer Leverett Professor of Physics

Acknowledgments

First and foremost, I would like to thank my mother for calling me at 7am every day during the pandemic in an attempt to get me to wake up earlier. I would also like to thank the other members of my family for not doing that. Thank you to Professor Mikhail Lukin for being a great advisor and giving me the opportunity to do work in such an interesting lab. Thank you to David, Ralf, and all the members of the SiV project for answering all my questions, being incredible sounding boards, and helping me find items in the ever-changing maze that is B16's drawer and shelving system. Thank you to Jackson, Chris, Sambuddha, and Gavin for constantly humbling me. Also, a quick thanks to Brandon, Emma, Noah, Austin, Aidan, Leon, Jill, Cassie, Will, Kyle, Gaby, Sara, Renée, Kidus, Natea, Aidan, and Jackson (again) for helping me graduate.

Contents

1 **Introduction and Context** **11**
  1.1 Quantum Repeaters 12
    1.1.1 Modern Communication Scheme using Repeaters 12
    1.1.2 Necessary Abilities 15
  1.2 Silicon Vacancy Center 19
    1.2.1 Repeater Scheme 20
  1.3 Heating Problem 24
    1.3.1 One-Qubit Gates 24

2 **Coplanar Waveguide Resonators** **27**
  2.1 Coplanar Waveguides 27
    2.1.1 Waveguide Derivation 28
    2.1.2 Resonators 31
  2.2 Microwave Driving 33
    2.2.1 Conductor Loss 35

3 **Superconducting Coplanar Waveguides** **37**
  3.1 Design and Simulation 37
  3.2 Superconducting Resonator Loss Channels 40
    3.2.1 Vortices 40
    3.2.2 Two-Level Defects 42

4 **Procedure** **45**

4.1 Fabrication 45
4.1.1 Sputtering 45
4.1.2 Lithography Process 46
4.2 Experimental Setup and Measurement 48
4.2.1 Iterations 48
4.2.2 Final Setup 48

5 Results and Conclusion **53**
5.1 Results 53
5.1.1 Measured Resonance with Continuous Driving 53
5.1.2 Pulsed Measurements 56
5.2 Conclusion and Future Work 57

List of Figures

1-1 Entanglement Distribution 13
1-2 Entanglement Distribution with a Quantum Memory 14
1-3 Entanglement Distribution in Series 14
1-4 Entanglement Purification 18
1-5 SiV Molecular Diagram 20
1-6 SiV Energy Level Diagram 21
1-7 SiV Spin-Photon Interface 22
1-8 Spin-Photon Coupling Procedure 22
1-9 Bell State Measurement Procedure 23
1-10 Heating and Power in SiV 25

2-1 Coplanar Waveguide Examples 27
2-2 Quarter Wave Resonator 28
2-3 Coplanar Waveguide Diagrams 29
2-4 Transmission and Reflection CPW Resonators 32
2-5 Simulated Resonance 32
2-6 Resonance Current 33
2-7 Magnetic field from CPW resonator at antinode. Figure reproduced from reference [21]. 35

3-1 Coplanar Waveguide Design for Simulation 39
3-2 Simulated Resonance for Two-Finger Resonator 40
3-3 Quality Factor and Coupling 41
3-4 Superconducting Phase Diagrams 41

3-5 Resistance at Vortex Phase 43
3-6 Boundaries of the Vortex Phase 43

4-1 Critical Temperature and Sputtering Pressure 46
4-2 Critical Temperature and Nitrogen 47
4-3 ODMR with Nitrogen Vacancy 48
4-4 Confocal Imaging of CPW 49
4-5 Resonator Design for Testing 49
4-6 Testing Environment 51

5-1 Nonlinear Response of NbTiN Resonator 54
5-2 Resonance Curve 55
5-3 Real and Imaginary Resonance 55
5-4 Resonance with Pulsed Measurements 57
5-5 Resonator Ramping 57

Chapter 1

Introduction and Context

The foundations of quantum mechanics were postulated in the early 20th Century, but only recently have scientists been able to use entanglement and wavefunction superpositions to their maximum capabilities. One process by which scientists have begun harnessing this power is quantum computing. Using the allowed interference and entanglement, quantum computers can theoretically execute some functions exponentially faster than their classical counterparts [1], [2], [3].

The power of this new computing increases every year, and recently, an experimental demonstration of its advantage has been performed (though doubts have begun to arise about the level of speedup and the functionality is, at its current level, not useful) [4], [5]. As the field grows, there too is a growing need for communication between computers. Quantum communication will allow for linking to form quantum computing clusters, as well as sending quantum data for other scientists to use in their experiments [6], [7].

More relevant, though, is quantum communication's impact on classical cryptography. Using a quantum channel, classical channel, and the no-cloning theorem, one can create a provably secure key for encoding and decoding some message through a public channel, a process called quantum key distribution (QKD). The first such scheme to do so was developed in 1984 by Bennett and Brassard (BB84) [8]. Since then, schemes with more relaxed conditions have been created.

However, quantum bits (qubits), travelling as photons, experience substantial loss on even the best optical fibers. Currently, the Corning SMF-28, a high-end optical fiber, has a loss of up to .32 dB/km [9]. Unfortunately, the no-cloning theorem prevents the use of classical repeaters, used to amplify the signal after fibre loss. This problem can be overcome with a quantum repeater, which will amplify and purify the correlation between remote communication partners.

The structure of this thesis will be as follows. First, the necessary components of a quantum repeater, along with a current quantum communication scheme using one, will be introduced. Second, a broad overview of the Silicon Vacancy architecture and its use as a repeater will be given. Next, we will discuss coplanar waveguide (CPW) resonators and how they can be improved using superconducting material. Finally, the procedure for creating these new striplines and the results arising will be presented.

1.1 Quantum Repeaters

Naively, one would attempt to replicate conventional repeater architecture. But this process is impossible for qubits. To boost a signal, the qubit would need to be measured and replicated, losing all quantum properties. Any scheme to do so without measurement violates the no-cloning theorem. We can, though, boost entanglement, which, in terms of QKD, is just as beneficial.

1.1.1 Modern Communication Scheme using Repeaters

A current state-of-the-art strategy for quantum communication is Measurement Device Independent QKD (MDI-QKD). The requirements of quantum repeaters for this scheme are the ability to do Bell-state measurements (BSM), entanglement purification, and a low-loss photon-memory interface. This scheme will be summarized, using figures from [6].

A key component of many QKD scheme is the distribution of entangled particles to two parties, commonly nicknamed Alice and Bob, across some distance. Without quantum repeaters, this distance is low, but the strategy is simple, as seen in Figure

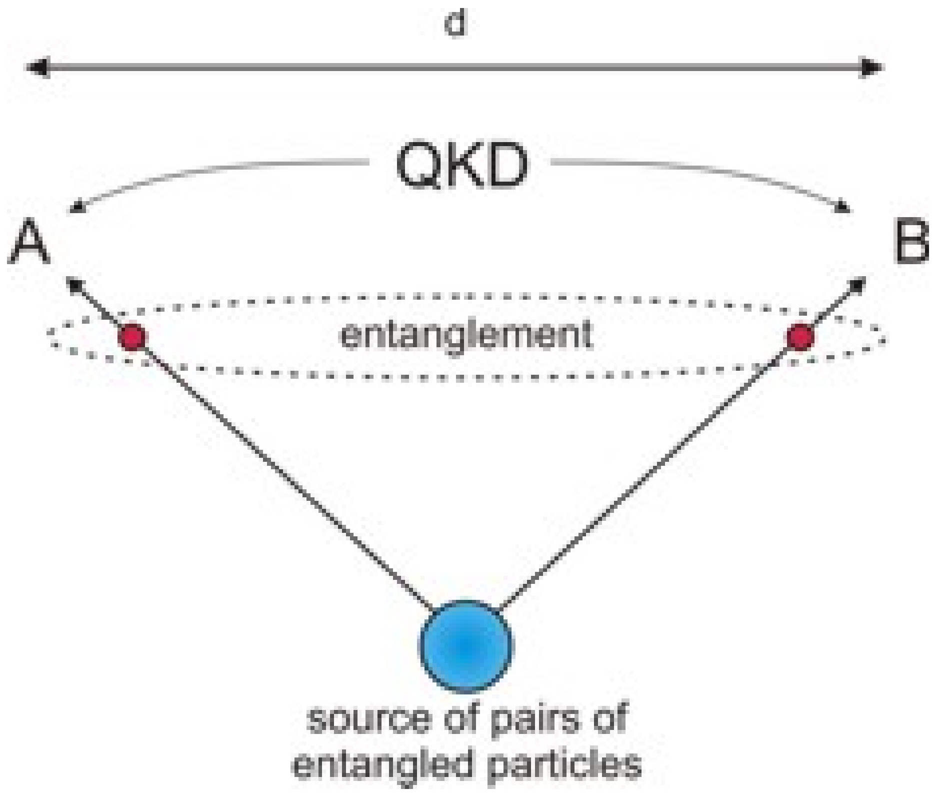

Figure 1-1: Distribution of two entangled particles from a single source. Figure reproduced from reference [6].

1-1. Using a source of entangled photons, we can transport them via an optical fibre to Alice and Bob. In this way, the two parties have qubits that will output the same state when measured.

For longer distances, a single source will not suffice. The fibres allow too much loss to recover any entanglement data. To increase the distance, we require an increase in entangled photon sources (Figure 1-2) [6]. With two sources, we can send photons to each party as well as a Bell-state measurement device. This device uses a measurement (described in BSM subsection below) to answer the question "are these particles identical?" without revealing their actual values.

Whether the answer is true or false, the measuring party now knows the correlation between the Alice and Bob's particles. This fails only when Alice and Bob have chosen different initial bases, making the BSM's answer meaningless. In addition, for these Bell-state measurements to work with linear optics, both photons must arrive in the device at the same time. This can be circumvented using a quantum repeater with

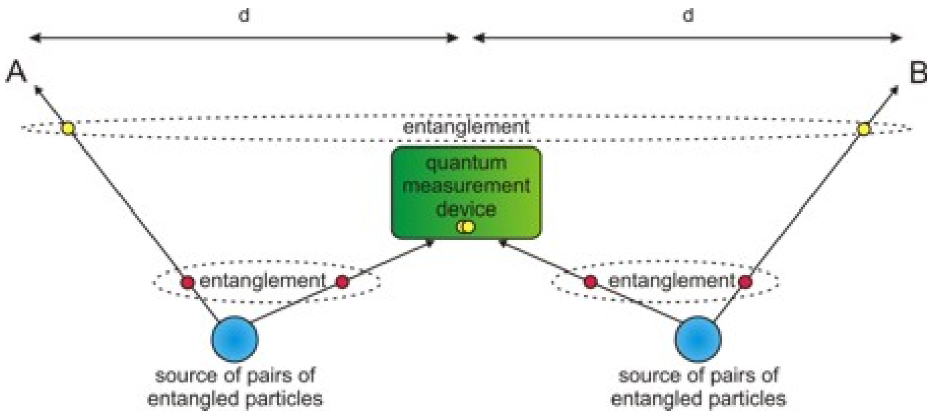
d
d
A
B
entanglement
quantum measurement device
entanglement
entanglement
source of pairs of entangled particles
source of pairs of entangled particles

Figure 1-2: Distributing entanglement across a larger distance.Figure reproduced from reference [6].

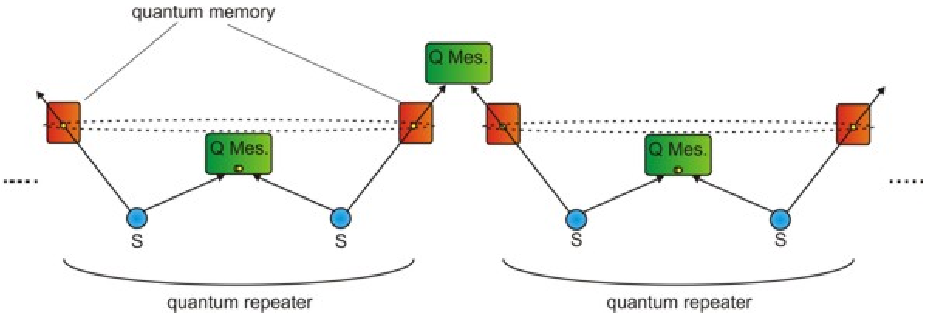
quantum memory
Q Mes.
Q Mes.
Q Mes.
.....
.....
S
S
S
S
quantum repeater
quantum repeater

Figure 1-3: Using a quantum memory to increase QKD efficiency.Figure reproduced from reference [6].

quantum memory.

By storing these entangled particles, as shown in Figure 1-3 [6], one can do asynchronous BSM's. This advantage becomes much more impactful as the chain of repeaters grows. While the chances of photons arriving at the same time can be high for one BSM, the chance that all photons arrive concurrently for a long string of BSM's will be very low. In this way, the quantum repeater links can wait as the rest of the chain starts to form, allowing the opportunity to consistently grow the entanglement, rather than wait on a 1 in a million chance.

1.1.2 Necessary Abilities

Bell-State Measurement

For the purposes of quantum communication, we need qubits that can be in one of four states: $|0\rangle$, $|1\rangle$, $|+\rangle$, or $|-\rangle$, where the relations between these states are defined in equation (1.1-4).

$$|+\rangle = \frac{|0\rangle + |1\rangle}{\sqrt{2}} \tag{1.1}$$

$$|-\rangle = \frac{|0\rangle - |1\rangle}{\sqrt{2}} \tag{1.2}$$

$$|0\rangle = \frac{|+\rangle + |-\rangle}{\sqrt{2}} \tag{1.3}$$

$$|1\rangle = \frac{|+\rangle - |-\rangle}{\sqrt{2}} \tag{1.4}$$

In our communication scheme, we have sources of entangled particles. This means that, given the measurement of one particle, we will know the state of the other. For two qubits, there are four states that maximally allow this, commonly known as Bell states [10].

$$|\Phi^+\rangle = \frac{|0\rangle_1|0\rangle_2 + |1\rangle_1|1\rangle_2}{\sqrt{2}} \tag{1.5}$$

$$|\Phi^-\rangle = \frac{|0\rangle_1|0\rangle_2 - |1\rangle_1|1\rangle_2}{\sqrt{2}} \tag{1.6}$$

$$|\Psi^+\rangle = \frac{|0\rangle_1|1\rangle_2 + |1\rangle_1|0\rangle_2}{\sqrt{2}} \tag{1.7}$$

$$|\Psi^-\rangle = \frac{|0\rangle_1|1\rangle_2 - |1\rangle_1|0\rangle_2}{\sqrt{2}} \tag{1.8}$$

Further, these states can be mixed, and we represent these mixtures with density matrices, defined below:

$$\rho = \sum_{n} |p_i \Psi_i\rangle\langle\Psi_i| \tag{1.9}$$

where n is the number of states mixed together. State mixture is not necessary for this process, but the structure of density matrices will be helpful.

Using this new approach, we can elucidate what entanglement does in the Bell states. For instance, given $|\Phi^+\rangle$, it can be shown that, dependent on measuring $|0\rangle$ on the first particle, the second will always measure as $|0\rangle$ (when in the same basis). Density matrices allow us to express this fact in the below equation.

$$\frac{Tr(\rho(M_{0_1} \otimes M_{0_2}))}{Tr(|\Phi^+\rangle\langle\Phi^+|M_{0_1} \otimes \mathbb{I})} = 1 \tag{1.10}$$

where

$$M_0 = |0\rangle\langle 0| \tag{1.11}$$

Using links of entangled sources and Bell state measurements, we want to create entanglement between some Alice and Bob. Given two entanglement sources in a series, we have 4 particles, and particles 2 and 3 go through a Bell-state measurement, which will entangle them dependent upon the success of the BSM. The state before measurement will look like so [10]:

$$|\Phi^+\rangle_{12} \otimes |\Phi^+\rangle_{34} = \frac{|0\rangle_1|0\rangle_2 + |1\rangle_1|1\rangle_2}{\sqrt{2}} \otimes \frac{|0\rangle_3|0\rangle_4 + |1\rangle_3|1\rangle_4}{\sqrt{2}} \tag{1.12}$$

$$= |\Phi^+\rangle_{14} \otimes |\Phi^+\rangle_{23} + |\Phi^-\rangle_{14} \otimes |\Phi^-\rangle_{23} + |\Psi^+\rangle_{14} \otimes |\Psi^+\rangle_{23} + |\Psi^-\rangle_{14} \otimes |\Psi^-\rangle_{23} \tag{1.13}$$

Pre-measurement, the state is completely mixed. It is only until after we clarify which Bell state particles 2 and 3 are in that entanglement is generated between the two sides. This process can be expanded past two sources, creating a near infinite-distance entanglement creator [6].

Entanglement Purification

But even along the short distances between repeaters, information is lost, resulting in finite infidelity. For an N link chain, our fidelity drops with F^N, such that we recover an exponential scaling of resources. Thus, it is necessary to create entanglement purification, which can correct the loss in fidelity which we label $(1-F)$. For simplicity, we only consider dephasing, rather than bit-flip errors [11].

$$\rho = F|\Phi^+\rangle\langle\Phi^+| + (1-F)|\Phi^-\rangle\langle\Phi^-| \tag{1.14}$$

To purify the entanglement, we must couple with another system of the same state [11].

$$\rho = (F|\Phi^+\rangle\langle\Phi^+| + (1-F)|\Phi^-\rangle\langle\Phi^-|)_{12} \otimes (F|\Phi^+\rangle\langle\Phi^+| + (1-F)|\Phi^-\rangle\langle\Phi^-|)_{34} \tag{1.15}$$

This algorithm involves a CNOT gate between qubits 1 and 3, a CNOT gate between qubits 2 and 4, measurements of qubits 1 and 2 on the X-axis, post-selection, and bit-flip. The CNOTs are done first and concurrently. After, the density matrix looks like so [11].

$$\begin{aligned} \rho_1 =& C_{13}C_{24}\rho C_{24}^\dagger C_{13}^\dagger = \\ & F^2|\Psi^+\rangle\langle\Psi^+| \otimes |\Phi^-\rangle\langle\Phi^-| \\ & + F(1-F)|\Psi^-\rangle\langle\Psi^-| \otimes |\Phi^+\rangle\langle\Phi^+| \\ & + F(1-F)|\Psi^-\rangle\langle\Psi^-| \otimes |\Phi^-\rangle\langle\Phi^-| \\ & + (1-F)^2|\Psi^+\rangle\langle\Psi^+| \otimes |\Phi^+\rangle\langle\Phi^+| \end{aligned} \tag{1.16}$$

For near-term devices, CNOT gates are complex and will add some noise to the system. Thus, it is cogent to say that each CNOT depolarizes with some probability p.

$$\rho \to (1-p)\rho + p\frac{1}{4}\mathbb{I}_{jk} \otimes \mathrm{tr}_{jk}(\rho) \tag{1.17}$$

Our new state after the CNOT gates is described below, after simplification.

$$\rho_2 = (1-p)^2\rho_1 + p(2-p)\frac{1}{16}\mathbb{I} \tag{1.18}$$

We then measure qubits 1 and 2 in the X-basis and confirm a match. If our state is described by ρ_1, the probability of success is $F^2 + (1-F)^2$. If it is completely mixed, our success rate is $\frac{1}{2}$. This gives a total purification chance of:

$$P = (1-p)^2(F^2 + (1-F)^2) + \frac{1}{2}p(2-p) \tag{1.19}$$

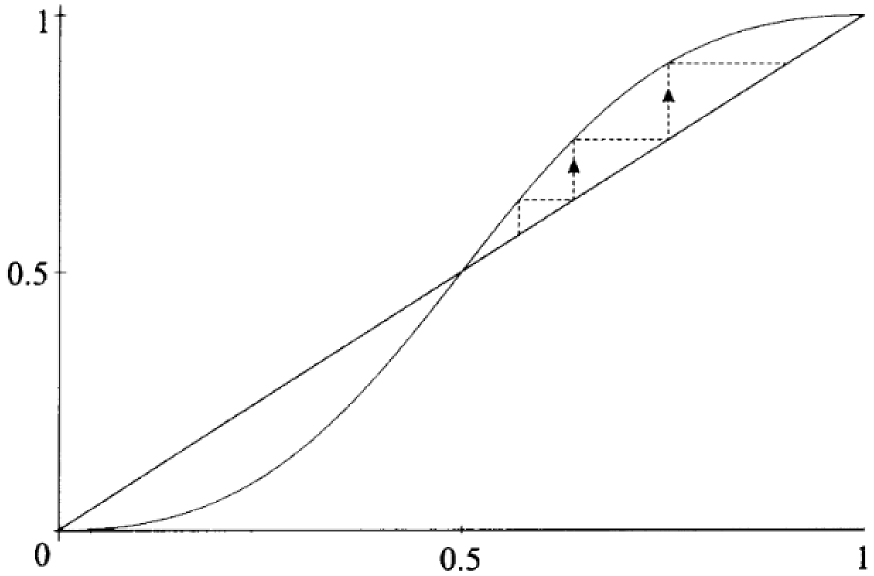

Figure 1-4: With F on the x-axis and F_1 on the y-axis, this graph shows how the steps of purification vary based on the original fidelity. For F lower than 1/2, the fidelity decreases. Figure reproduced from reference [12].

After a bit-flip, our density matrix is now [11]

$$\rho_3 = \frac{(1-p)^2F^2|\Psi^-\rangle\langle\Psi^-| + (1-p)^2(1-F)^2|\Psi^+\rangle\langle\Psi^+| + \frac{1}{2}p(2-p)\frac{1}{4}\mathbb{I}}{(1-p)^2(F^2+(1-F)^2) + \frac{1}{2}p(2-p)} \tag{1.20}$$

Thus, our fidelity to $|\Psi^-\rangle\langle\Psi^-|$ grows.

$$F_1 = \frac{(1-p)^2F^2 + \frac{1}{2}p(2-p)\frac{1}{4}}{(1-p)^2(F^2+(1-F)^2) + \frac{1}{2}p(2-p)} \tag{1.21}$$

By solving the equation $F = F_1 = F_{max}$, we can find the maximum amount entanglement purification can increase the fidelity. It turns out that there are restrictions. Unless $F_{original} > 1/2$ and $p < 1 - 1/\sqrt{2}$, the fidelity can actually decease. Barring that, our maximum after many iterations is [11]

$$F_{max} = \frac{1}{2}(1 + \frac{\sqrt{1-4p+2p^2}}{1-p}) \tag{1.22}$$

For $p = 0$, a visual representation of purification can be seen in Figure 1-4 [12].

Photon-Memory Interface

A third necessary component is an efficient interface between the photons of an entanglement source and the memory used to facilitate asynchronous Bell state measurements. There are many different methods, such as optical ring resonators or weak coherent pulses separated in time. But in the end, we would like the information stored in photons to be stored in our logical space. This photonic quantum information is usually stored via polarization angles. The states we need are horizontal, vertical, diagonal, and anti-diagonal.

$$|D\rangle = \frac{|H\rangle + |V\rangle}{\sqrt{2}} \tag{1.23}$$

$$|A\rangle = \frac{|H\rangle - |V\rangle}{\sqrt{2}} \tag{1.24}$$

$$|H\rangle = \frac{|D\rangle + |A\rangle}{\sqrt{2}} \tag{1.25}$$

$$|V\rangle = \frac{|D\rangle - |A\rangle}{\sqrt{2}} \tag{1.26}$$

1.2 Silicon Vacancy Center

The Silicon Vacancy Center (SiV) in diamond is the architecture for quantum repeaters used in this thesis. Diamond consists of covalently-bonded carbon atoms in a cubic lattice structure. A vacancy center is an impurity in diamond where carbon atoms are replaced by other particle, creating a hole that should have an electron. In the case of SiV, this particle is silicon [13].

In the SiV center (shown in Figure 1-5) [13], a silicon atom takes the place of two carbon atoms, sitting in between the two spots. This creates a split vacancy (transparent) and the nearby carbon atoms (shades of blue) interact with the hole spin through unsaturated bond orbitals.

The SiV center is characterized by its bright, narrow optical transitions between excited state (called LB') and ground state, as in Figure 1-6. The ground state is

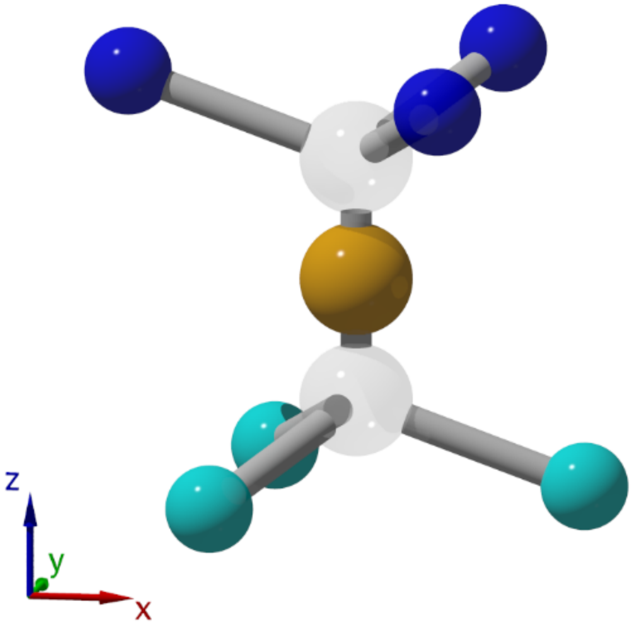

Figure 1-5: Silicon Vacancy Center molecular diagram. Figure reproduced from reference [13].

split by crystal strain into two branches (UB and LB), where only LB is used for logical operation and UB is only entered as error from phonon interactions. Further, each branch is composed of two spin sublevels created by spin-orbit coupling [13].

Previously, the error caused by phonon-UB interactions limited quantum memory in the color center. Findings by the Lukin Group's quantum repeater lab have concluded, though, that operating at 100mK (instead of 4K) reduces the amount of requisite error phonons and increases this memory time to over 10ms, long enough for repeater operations [14].

Our quantum operation relies on lifting degeneracy by applying a magnetic field using the zeeman-split levels. Spin-conserving optical transitions are also split, such that a single transition, $|\downarrow\rangle$ to LB', can be addressed.

1.2.1 Repeater Scheme

A SiV quantum repeater, at its base, needs to take asynchronous photons from two sources, Alice and Bob (A/B), and perform a Bell state measurement. In this setup,

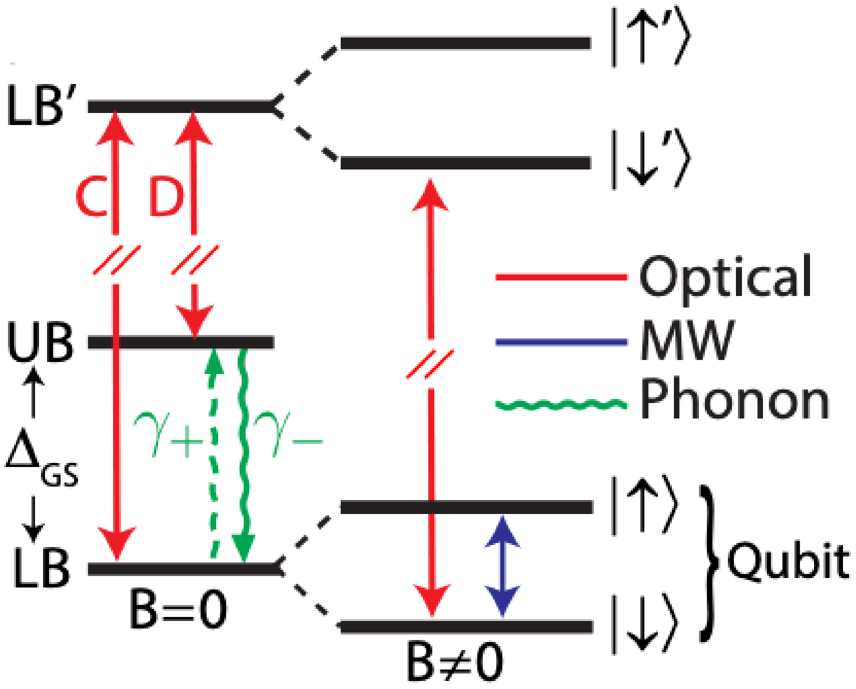

Figure 1-6: Silicon Vacancy Center energy level diagram. Figure reproduced from reference [14].

the information is encoded in a superposition of an early and late photon, separated by some time δt. Using measurement and post-selection, we can transmit this information to our spin system.

Our SiV system starts in $|\uparrow\rangle$. Following the procedure in Figure 1-8, we rotate to $|\uparrow\rangle + |\downarrow\rangle$, making our spin/photon system wavefunction as below [15]:

$$|\Psi\rangle = (c_e|e\rangle + c_l|l\rangle) \otimes (|\downarrow\rangle + |\uparrow\rangle) \tag{1.27}$$

$$|\Psi\rangle = c_e|e\uparrow\rangle + c_e|e\downarrow\rangle + c_l|l\uparrow\rangle + c_l|l\downarrow\rangle \tag{1.28}$$

We condition the success of this operation on detection of a photon at the end. As there is no reflection when in $|\downarrow\rangle$, we know the SiV must be in $|\uparrow\rangle$ upon arrival of the early photon [15].

$$|\Psi\rangle = c_e|e\uparrow\rangle + \cancel{c_e|e\downarrow\rangle} + c_l|l\uparrow\rangle + c_l|l\downarrow\rangle \tag{1.29}$$

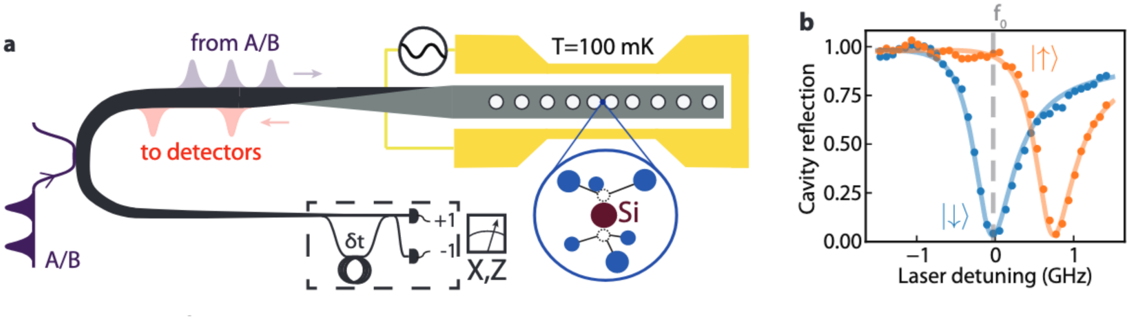
a
from A/B
to detectors
A/B
T=100 mK
δt
+1
-1
X,Z
Si
b
f0
1.00
0.75
0.50
0.25
0.00
Cavity reflection
|↑⟩
|↓⟩
−1
0
1
Laser detuning (GHz)

Figure 1-7: **a.** A diagram of the photon-spin interface electronics **b.** If the SiV is in $|\uparrow\rangle$, the photon is reflected. Figure reproduced from reference [15].

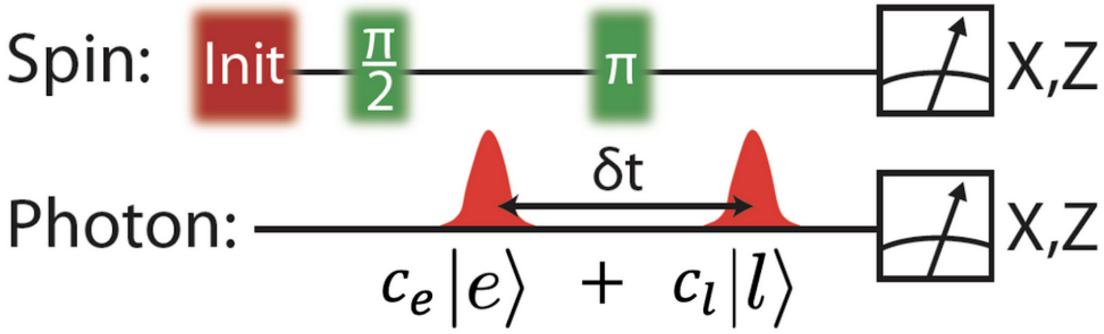
Spin:
Init
π/2
π
X,Z
δt
Photon:
X,Z
c_e|e⟩ + c_l|l⟩

Figure 1-8: Procedure for spin-photon coupling. Figure reproduced from reference [15].

After the Pi-pulse between the two photons, our wavefunction looks like so:

$$|\Psi\rangle = c_e|e\downarrow\rangle + c_l|l\downarrow\rangle + c_l|l\uparrow\rangle \tag{1.30}$$

Once again, due to success conditioning, we know the SiV must be in $|\uparrow\rangle$ upon arrival of the late photon.

$$|\Psi\rangle = c_e|e\downarrow\rangle + \cancel{c_l|l\downarrow\rangle} + c_l|l\uparrow\rangle \tag{1.31}$$

We have now transferred information between the photon and spin-system.

$$|\Psi\rangle = c_e|e\downarrow\rangle + c_l|l\uparrow\rangle \tag{1.32}$$

Further, there is a loop of wire that closes the δt gap between photon pulses, such that we do not know whether the early or late pulse is detected. Therefore our wavefunction will not collapse further. Upon viewing of this wavefunction in the X-basis, it becomes obvious that an X-measurement on the photon differentiates between the two states $c_e|\downarrow\rangle \pm c_l|\uparrow\rangle$.

$$|\Psi\rangle = |+\rangle(c_e|\downarrow\rangle + c_l|\uparrow\rangle) + |-\rangle(c_e|\downarrow\rangle - c_l|\uparrow\rangle) \tag{1.33}$$

This will be used in the BSM procedure given two of these photon pairs, seen in Figure 1-9.

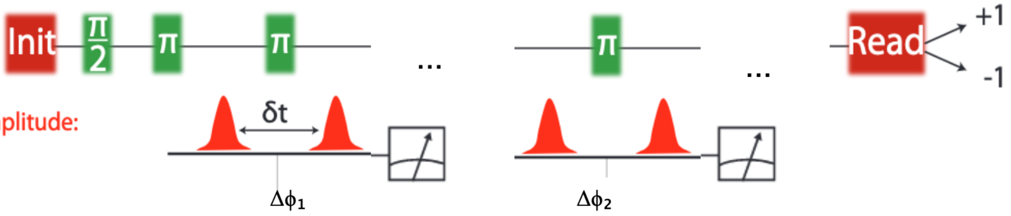

Figure 1-9: Procedure for Bell state measurement between two sources.

After the first photon pair and an output m_1 from our photon X-measurement, we have a state:

$$|\Psi\rangle = |\downarrow\rangle + m_1 e^{i\phi_1}|\uparrow\rangle \tag{1.34}$$

The second photon pair and measurement gives us:

$$|\Psi\rangle = |\downarrow\rangle + m_1 m_2 e^{i(\phi_1+\phi_2)}|\uparrow\rangle \tag{1.35}$$

We then measure the spin in the X-basis, giving us an m_3 where [15]

$$m_1 m_2 m_3 = e^{i(\phi_1+\phi_2)} = \pm 1 \tag{1.36}$$

Dependant on inputting the same axes, we now know the relation between Alice and Bob's photons without knowing their actual values, realizing a BSM.

1.3 Heating Problem

The SiV quantum repeater architecture is highly developed and experimentally demonstrated. But it currently has a problem: heating. The gold stripline, as mentioned before, dissipates heat when driving microwaves. Some of this heat finds the SiV center. This heating problem is most experimentally seen in long sequences of MW pulses, where it induces decoherence in the spin system. But also notable is how it limits the SiV's ability to perform two-qubit gates. The power required and subsequent error caused is so high as to completely prevent them [16].

1.3.1 One-Qubit Gates

We can model the SiV center's suspended cavity as a 1-D rod in a thermal bath (carbon atoms). Microwave pulses heat the bath, thermalize the rod, and cool down at a rate set by τ_{th}, characterized by the diamond's conductance and the SiV's geometry. From [16], an equation for the rod's heating is found:

$$T_{SiV} \propto e^{-(t-t_0)/\tau_{th}} - e^{9(t-t_0)/\tau_{th}} \tag{1.37}$$

This heating is small for short times between pulses ($\tau < \tau_{th}$) and for long gaps ($\tau >> \tau_{th}$). For intermediate times, there is not enough time for the heat to dissipate between pulses, and heat begins to build up.

This seems ideal, as it is best for pulse sequences to be as fast, to do as much as possible before decoherence. But the pulse gaps are determined by the rabi oscillation frequency, which scales with the square root of power, increasing the heating within the system substantially [16].

$$\Omega_R \approx \sqrt{P} \tag{1.38}$$

Optimizing between heating and decoherence, we find the fastest our gates can operate is $\tau = 70\ \mu s$. For advanced quantum information processing, we need many more pulses, ideally at a high power, to accomodate for zeeman fluctuations. This operation will increase temperature enough to cause decoherence in our current setup.

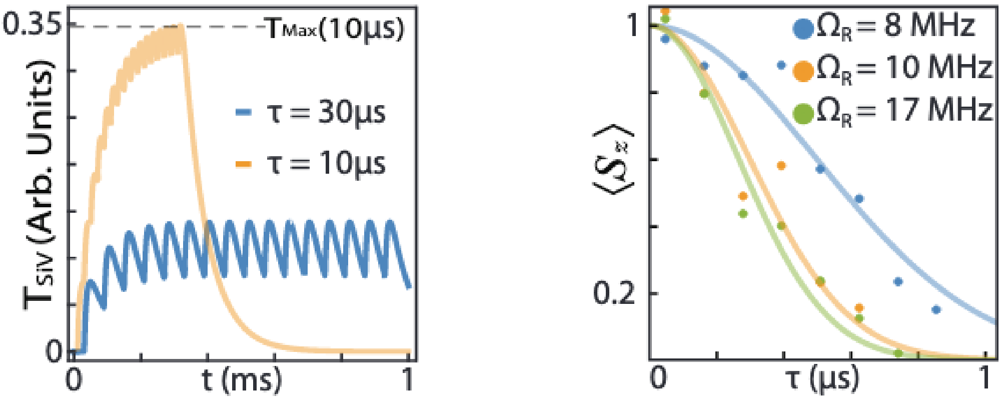

(a)

(b)

Figure 1-10: **a.** Relation between pulse gap time and temperature. **b.** The effect of Rabi frequency on coherence times. Figures reproduced from reference [16].

Chapter 2

Coplanar Waveguide Resonators

2.1 Coplanar Waveguides

A waveguide is a structure that can be used to transmit electromagnetic waves across some medium with relatively low loss. Examples include optical fibers, which are widely used to transfer network data, and transmission lines, which are needed for carrying high-frequency current. Coplanar waveguides are a unique form of transmission line where all features are 2D and can be easily printed using current lithography techniques. The waveguide consists of three narrow bands of conductor separated by capacitive gaps and surrounded by dielectrics. A basic example cross-section can be found in Figure 2-1(a).

In this chapter, we will be laying down the math required to understand the

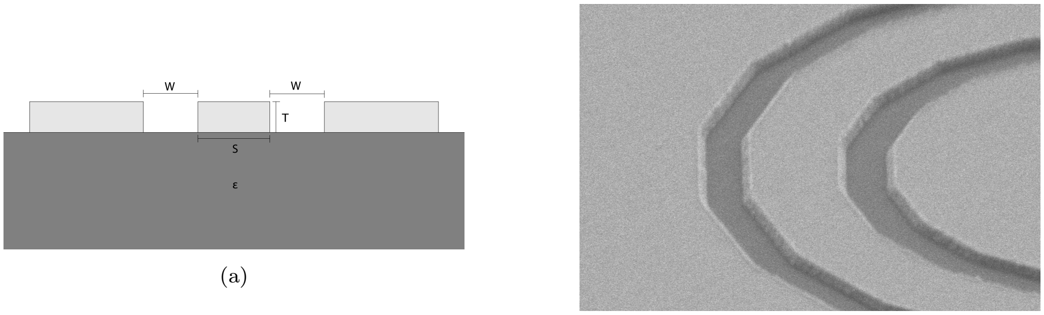

(a)

(b)

Figure 2-1: **(a)** Cross section of a coplanar waveguide on a dielectric. **(b)** Electron microscope image of a NbTiN CPW stripline from above.

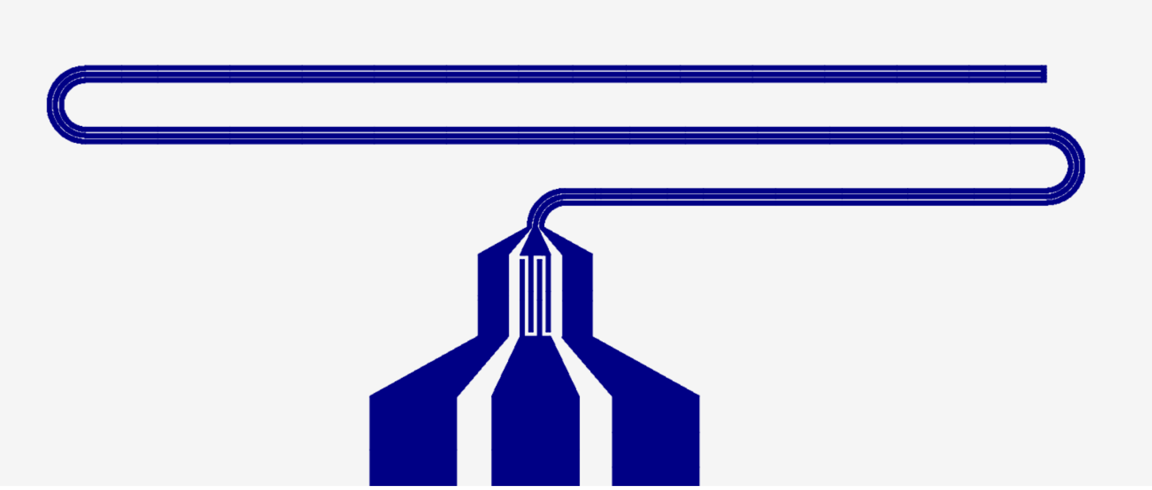

Figure 2-2: A quarter-wave ($\lambda/4$) center-conductor capacitively-coupled coplanar waveguide resonator structure.

characteristics, uses, and inefficiencies of the quarter-wave ($\lambda/4$) center-conductor capacitively-coupled coplanar waveguide resonator structure that we will use for the results of this thesis, as seen in Figure 2-2.

2.1.1 Waveguide Derivation

To fully characterize a coplanar waveguide, we need to know the effective dielectric constant (ϵ_{eff}) and characteristic impedance (Z_0). The full diagram of any CPW can be found in Figure 2-3, as seen in [17]. In this CPW structure, there can be dielectric material on either side of the stripline, as well as shielding conductors some distance away.

Using the conformal analysis strategem defined in [18], the capacitance between conductor lines can be represented as a series of layer-defined dielectric-filled parallel plate capacitors:

$$C_{cpw} = C_{air} + C_1 + C_2 \tag{2.1}$$

C_1 and C_2, in this equation, are the capacitances of the top and bottom dielectrics. Further, the definition of a parallel plate capacitor tells us (2.2), which give us an expression for ϵ_{eff} (2.3):

$$C_{cpw} = \epsilon_{eff} C_{air} \tag{2.2}$$

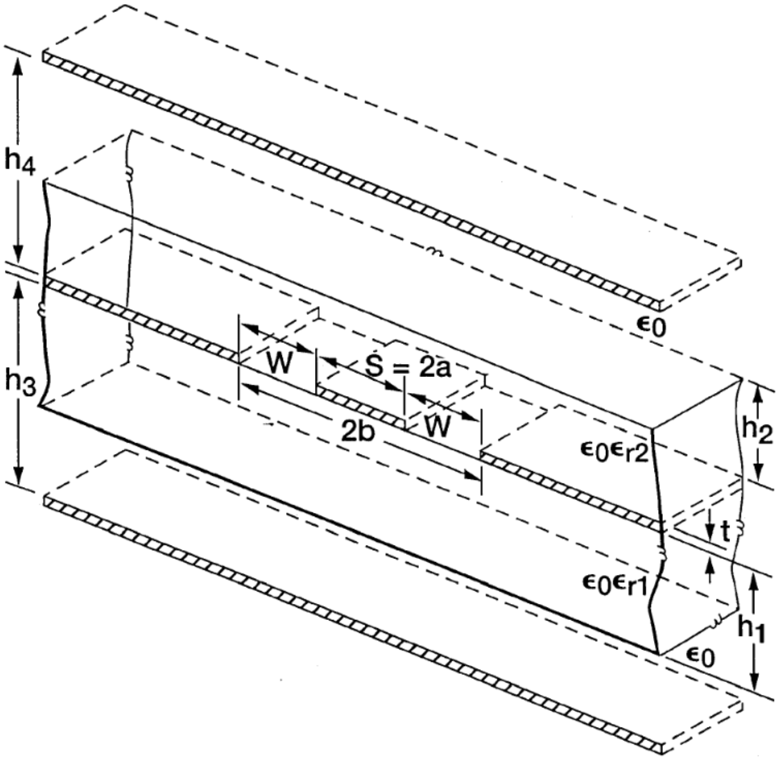
h4
h3
W
S = 2a
2b
W
ε0
h2
ε0εr2
t
ε0εr1
h1
ε0

Figure 2-3: A more complete diagram of coplanar waveguides. Figure reproduced from reference [17].

$$\epsilon_{eff} = 1 + \frac{C_1 + C_2}{C_{air}} \tag{2.3}$$

The same conformal mapping gives us equations for the dielectric capacitances [17].

$$C_i = \epsilon_{r_i}\epsilon_0 \frac{K(k_i)}{K(k_i')}, \quad i = 1, 2 \tag{2.4}$$

$$C_{air} = 2\epsilon_0 \frac{K(k_{air})}{K(k_{air}')} \tag{2.5}$$

where K(k) is the complete elliptical integral and its moduli are:

$$k_i = \frac{sinh(\frac{\pi s}{2h_i})}{sinh(\frac{\pi(s+2w)}{4h_i})} \tag{2.6}$$

$$k_{air} = \frac{tanh(\frac{\pi s}{2h_{air}})}{tanh(\frac{\pi(s+2w)}{4h_{air}})} \tag{2.7}$$

$$k_i' = \sqrt{1 - k_i^2}, \quad i = 1, 2, \text{air} \tag{2.8}$$

This gives us all we need to calculate ϵ_{eff}, as well as Z_0. The formula for characteristic impedance of a electromagnetic waveguide is well known, and we can adapt it to our structure [17].

$$Z_0 = \frac{\sqrt{\epsilon}}{Cc}, \text{ where c is the speed of light} \tag{2.9}$$

$$Z_0 = \frac{\sqrt{\epsilon_{eff}}}{C_{cpw}c} \tag{2.10}$$

$$Z_0 = \frac{1}{\sqrt{\epsilon_{eff}}C_{air}c} \tag{2.11}$$

Luckily, our CPW striplines are significantly less complicated and look more similar to Figure 2-1 (no shielding conductors or top dielectric, semi-infinite bottom dielectric). Thus, we can make approximations: $h_1 \to \infty$, $\epsilon_{r_2} = 1$, $h_3 = h_4 \to \infty$, dependence on h_2, k_2 disappears. Our equations begin to simplify [17].

$$k_1 = k_{air} = k = \frac{s}{s + 4w} \tag{2.12}$$

$$C_{cpw} = C_{air} + C_1 \tag{2.13}$$

$$k'_1 = k'_{air} = k' = \sqrt{1-k^2} \tag{2.14}$$

$$C_1 = \epsilon_{r_1}\epsilon_0 \frac{K(k)}{K(k')} \tag{2.15}$$

$$C_{air} = 2\epsilon_0 \frac{K(k)}{K(k')} \tag{2.16}$$

We can then plug (2.15) and (2.16) into equation (2.13) and get a short and elegant equation for ϵ_{eff}.

$$C_{cpw} = (\epsilon_{r_1} + 2)\epsilon_0 \frac{K(k)}{K(k')} \tag{2.17}$$

$$\epsilon_{eff} = \frac{(\epsilon_{r_1} + 2)}{2} \tag{2.18}$$

Plugging our new information into (2.11), we find a simplified Z_0, though it still requires a complete elliptical integral.

$$Z_0 = \frac{30\pi}{\sqrt{\frac{(\epsilon_{r_1}+2)}{2}}} \frac{K(k)}{K(k')} \tag{2.19}$$

Most microwave equipment uses a characteristic impedance of 50Ω. Lack of impedance matching leads to unwanted reflections and loss, so we must solve this equation on a silicon-doped diamond substrate to find S and W values. We find [19]:

$$S \approx 1.5W \tag{2.20}$$

2.1.2 Resonators

Resonances occur in waveguides when the structure allows for the creation of a standing wave at certain frequencies. In the case of coplanar waveguides, this situation arises when the reflective waves from a capacative gap and/or short interfere exactly. There are two commonly used structures for creating these resonances, which can be found in Figure 2-4. The two differ on which scattering parameter the resonance can be found, S_{11} or S_{21}.

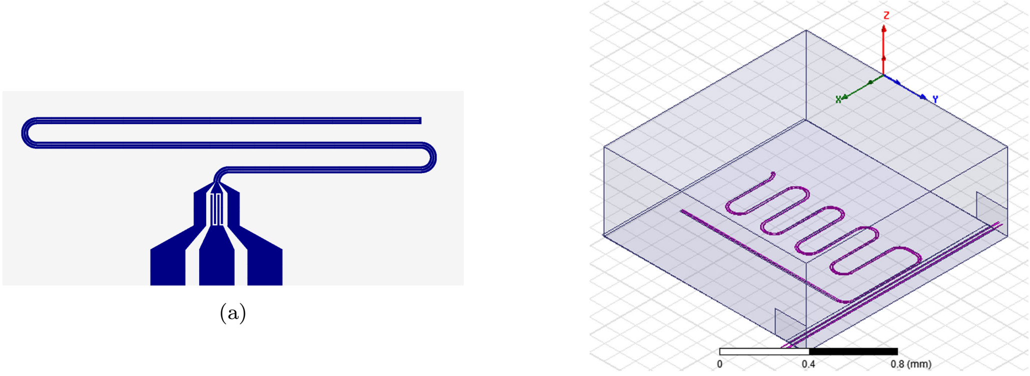

(a)

(b)

Figure 2-4: **(a)** S_{11}-type resonator. **(b)** S_{21}-type resonator.

With the first structure, the capacitor is found in the middle conductor. Thus, current is only transmitted across when a standing wave is formed. In this case, the reflection at the capacitor dips, giving us a typical resonance response graph as in Figure 2-5. This reflection begins and ends at the input port so is called S_{11}.

The second type positions the capacitor between two different coplanar waveguides. In this case, energy is only transferred to the second CPW at a resonance. This causes a dip in the transmission from port 1 to port 2, thus S_{21}.

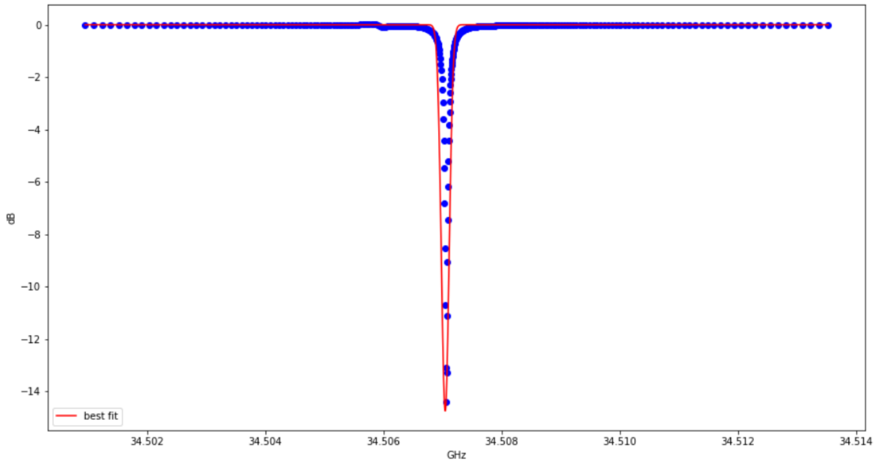

Figure 2-5: A simulated response dip at a resonance.

The frequency at which resonances occur can be found in the familiar standing wave equation [20].

$$f_r = \frac{c_m}{4l}(2p-1) \tag{2.21}$$

where c_m is the speed of light in the medium, which we have calculated:

$$c_m = \frac{c}{\sqrt{\epsilon_{eff}}} \tag{2.22}$$

The range of frequencies that can create a resonance is measured by the Q-factor, which is the resonant frequency divided by the full-width half-max (FWHM) of the dip.

$$Q = \frac{f_r}{\Delta f} \tag{2.23}$$

This quality factor can then be split into two components, external and internal, as shown in equation 2.23. Internal Q accounts for losses from intrinsic characteristics of the conductor and dielectric. External Q accounts for loss from radiation or coupling [20].

$$\frac{1}{Q} = \frac{1}{Q_i} + \frac{1}{Q_e} \tag{2.24}$$

Though Q_i is constant, we can change Q_e by modifying the capacitance used for creating the resonators. In this application, we want a relatively high Q_e to allow for microwave driving.

2.2 Microwave Driving

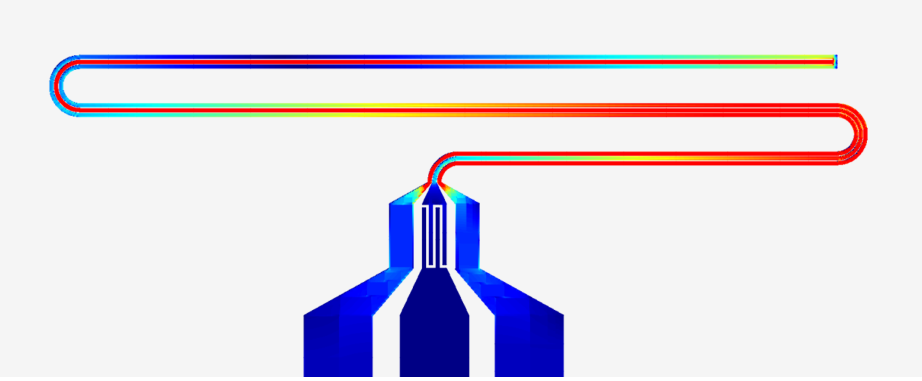

Figure 2-6: Standing wave current at resonance.

Due to the creation of a standing wave, the microwave current varies based on location on the resonator, as in Figure 2-6 and equation 2.24.

$$I(l) = I_0 cos(2\pi \frac{l}{\lambda_0}) \tag{2.25}$$

In this equation, I_0 is the maximum current (at the antinodes) and λ_0 is the resonant frequency [21].

We need to use this current to calculate the electromagnetic coupling rate between waveguide and vacancy center. This will be done by calculating the current needed to produce one photon at the vacany's driving frequency. By definition, this is the average zero-point current I_{zpf}. The necessary energy is produced by the inductance of our circuit:

$$E = LI_{zpf}^2 \tag{2.26}$$

We must then integrate over the entire circuit (we will use quarter-wave), using the derived standing wave current.

$$E = \int_0^{\lambda_0/4} LI_{zpf}^2 cos(2\pi \frac{l}{\lambda_0})^2 dl \tag{2.27}$$

This is equivalent to the energy of a vacancy-frequency photon [21].

$$\hbar\omega_{vac} = \frac{\lambda_0}{4} LI_{zpf}^2 \tag{2.28}$$

Rearranging, we find the necessary current.

$$I_{zpf} = 2\sqrt{\frac{\hbar\omega_{vac}}{\lambda_0 L}} \tag{2.29}$$

This current is then used to calculate the magnetic field at the vacancy and surrounding areas. This is done using the Biot-Savart Law for any point $\mathbf{r}$ (2.29). Hatermann, Fortagh gives a good visual for this field in Figure 2-7 [21].

$$B_{ph}(\mathbf{r}) = \frac{\mu_0}{4\pi} \int\int\int_{CPW} \frac{(\mathbf{I}_{zpf} dV) \times \mathbf{r}}{|\mathbf{r}|^3} \tag{2.30}$$

We can then find the coupling rate using the formula for the energy of a magnetic moment in a field and dividing by Planck's Constant [21].

$$g = \frac{|\mathbf{B}_{ph}(r)| \cdot |\mu|}{\hbar} \tag{2.31}$$

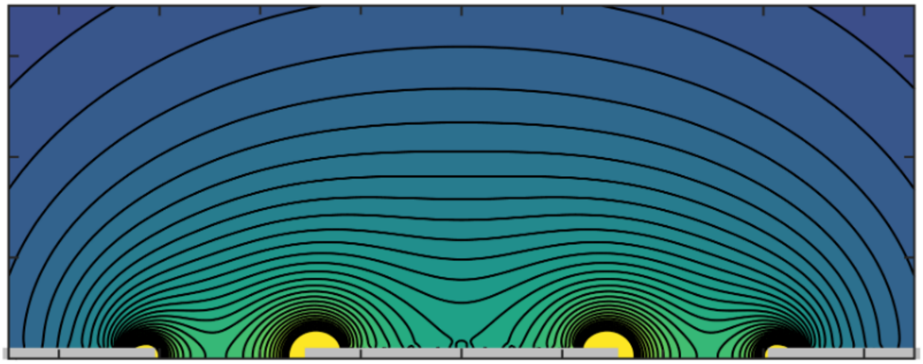

Figure 2-7: Magnetic field from CPW resonator at antinode. Figure reproduced from reference [21].

2.2.1 Conductor Loss

There are three types of signal loss that can occur in a CPW: dielectric, conductor, and radiation. Dielectric relaxation occurs at much higher frequencies, so dielectric loss is much lower than the other two types in our experiment.

Radiation loss describes electromagnetic energy leaking into the dielectric, and is the medium which we use to couple to our vacancy center. Thus, this type of loss will not hurt the efficiency of our coplanar waveguide.

Conductor loss is the attenuation caused by the resistance of the stripline material. This loss is not beneficial, increasing the necessary power and, in turn, heating the system and causing error. As given in [22], the equation for conductor loss is:

$$\alpha_c = 4.88 \times 10^{-4} R_s \epsilon_{eff} Z_0 \frac{P'}{\pi W}(1 + \frac{S}{W})(\frac{\frac{1.25}{\pi} ln\frac{4\pi S}{T} + 1 + \frac{1.25T}{\pi S}}{(2 + \frac{S}{W} - \frac{1.25T}{\pi W}(1 + ln\frac{4\pi S}{T}))^2}) \tag{2.32}$$

In this equation, R_s is the surface resistivity and P' is a constant inherent to the geometry. Though the entire equation is not important, the loss increases with surface resistivity and as the stripline's features grow smaller. Due to the requisite nanometer scale of the CPW, this attenuation can be large. The current stripline material is gold. At 1K, it has a surface resistivity of .22 $\Omega \cdot nm$.

Below critical temperature, superconductors have 0 surface resistivity, eliminating conductor loss and creating a marked increase in resonator efficiency. The next chapter will further discuss the design and properties of superconducting striplines.

Chapter 3

Superconducting Coplanar Waveguides

A coplanar waveguide (CPW) is used in our quantum repeater scheme to drive rotations in the silicon vacancy's solid-state qubit. Though all CPW resonators will be able to drive to some degree, their ability is largely determined by the material properties and design. Goals include formulating the resonators to a certain amplification, frequency, and percentage loss. Further, though superconducting resonators demonstrate a clear advantage over previous materials, they too present obstacles that must be taken into consideration [23], [24].

3.1 Design and Simulation

The designs for the superconducting stripline project were created using GDSpy, a python module that allows for the construction of GDS files using polygons and boolean arithmetic. The GDS files were then simulated with microwave frequency ports in Sonnet Electromagnetic Suites to test for resonances, coupling, and magnetic field.

As mentioned in Chapter 2, most microwave technology operates at 50 Ω characteristic impedance. This allows for near-zero reflectivity between devices, which is beneficial as this interference can cause noise in whatever data is being transferred. So we must make sure our microwave resonator also has this impedance. This is ensured through calculating the conductor-gap ratio for our setup. As above, we find:

$$S \approx 1.5W \tag{3.1}$$

where S is the width of the center conductor and W is the width of the gaps in between.

Further, the frequency of our resonator must be in the microwave regime. This falls between 300 MHz to 300 GHz, though solid-state vacancy spin physics usually operates on the order of 1-20 GHz, and as such, many of our devices can only work in this range. Therefore our resonances must be in this frequency range as well.

However, these frequencies can require very long resonator lengths (relative to nanofabrication). A frequency of 1 GHz has a wavelength of 300mm in vacuum, which is much too long for the surface of a diamond. One way to mollify this requirement is the use of a $\lambda/4$ CPW geometry, which only requires a quarter wavelength. Operating at our ideal 10 GHz in this structure requires only 7.5mm.

For simulation, though, we do not need anything even this long. This microwave engineering is scale invariant, given some rescaled length and inversely scaled frequency. Specifically, the same physics at 7.5mm works at 1-2mm, and with much less computational cost. Thus, our simulations are in this regime, and we use the geometry pictured in Figure 3.1.

This resonator's length is approximately 1.9mm, so due to the resonator's quarter wave nature, it's resonance is around 38 GHz.

An important characteristic to analyze for any resonance is its quality-factor, a constant for some geometry and setup that describes the total loss of the system. For this system, this quality factor is split into intrinsic (loss from the resonator, Q_i) and extrinsic (loss due to capacative coupling, Q_e). In any resonator, the quality factor scales with the sharpness and amplitude of the resonant dip.

$$\frac{1}{Q} = \frac{1}{Q_i} + \frac{1}{Q_e} \tag{3.2}$$

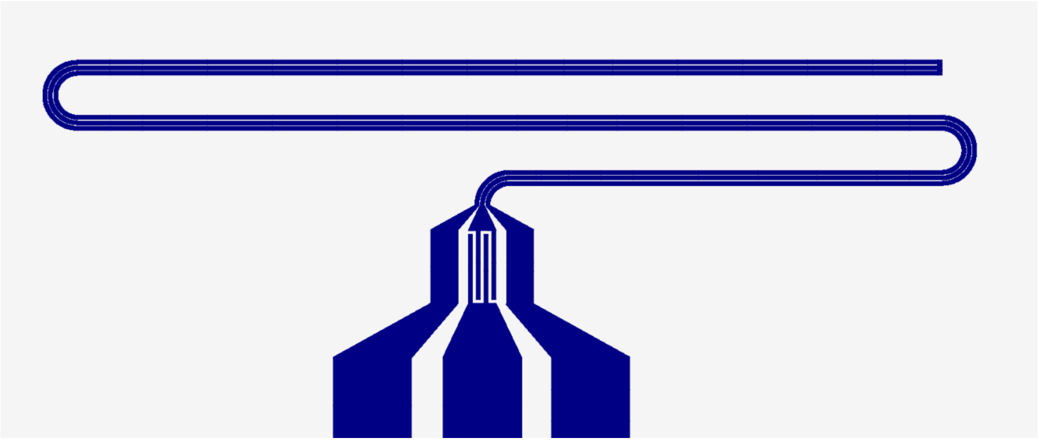

Figure 3-1: A quarter-wave ($\lambda/4$) center-conductor capacitively-coupled coplanar waveguide resonator structure.

We split this relation into three regimes. When intrinsic loss dominates ($Q_i >> Q_e$), the resonator is undercoupled. When extrinsic dominates ($Q_e >> Q_i$), it is overcoupled. When the two are about the same, it is called critically coupled [20].

Further, it is possible to increase Q_e by increasing the capacitance at our coupling component. This phenomenon is mapped in the above geometry, in order to find critical coupling, by varying the number of capacative fingers. The results were simulated and can be found in the table below and Figure 3-3.

Fingers	Q	Resonance Amplitude (dBm)	Resonance Freq. (GHz)
1	5127800	-1.438	39.182
2	4919297	-0.839	38.207
3	2612132	-0.540	36.927
4	1106289	-7.793	35.678
5	393098	-14.414	34.507

But the intrinsic Q does not solely account for the resonator's coupling to the SiV. There are unwanted loss channels, such as dissipation from vortex motion, as well as two-level defect loss [25].

$$\frac{1}{Q_i} = \frac{1}{Q_v} + \frac{1}{Q_{rad}} + \frac{1}{Q_{TLS}} \tag{3.3}$$

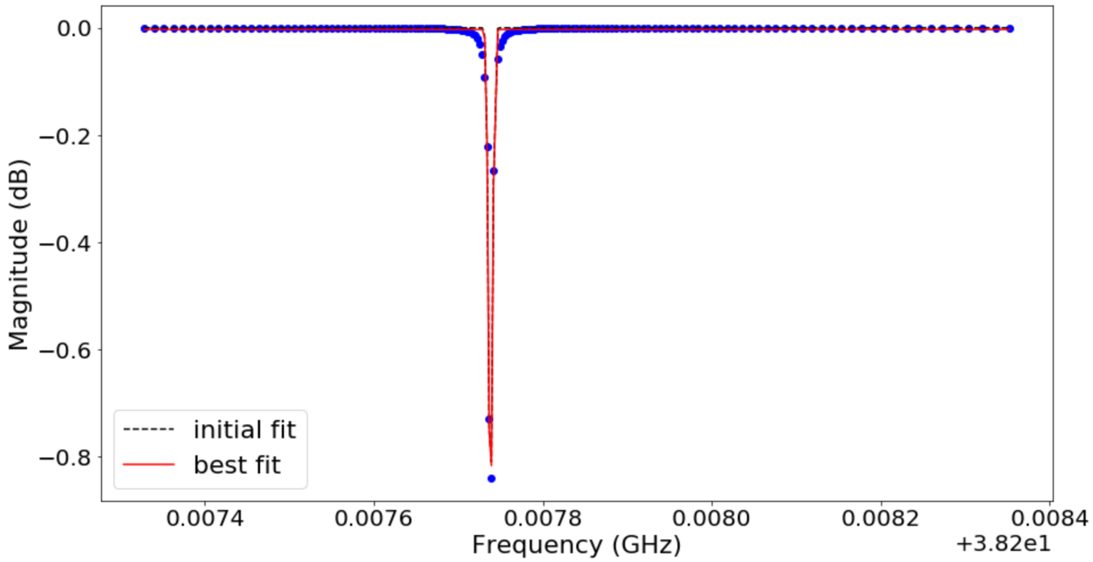

Figure 3-2: Resonance for above design

3.2 Superconducting Resonator Loss Channels

3.2.1 Vortices

For all superconductors, there are characteristic lengths called the penetration depth and the coherence length. Penetration depth measures the length that a magnetic field can penetrate a superconductor. Coherence length measures the smallest length that a change can occur at in a superconductor without breaking its superconductivity.

In type II superconductors, the coherence length is less than the penetration depth, which would create an unstable system. This problem is solved by a macroscopic, quantum phenomenon called vortices [26]. Vortices form in a phase between perfect superconducting and their breaking point, where a small amount of magnetic flux is allowed to penetrate into the metal. Because of this imperfect phase, superconductors of this type can exist in higher magnetic fields, an important property that factored in to our lab's decision to pick NbTiN. This phase is pictured in Figure 3-4.

The points in which magnetic flux enters the superconductor is called a vortex. Due to this magnetic flux, the current density increases as it approaches the center, simultaneously increasing the kinetic energy of the cooper pairs involved. At a certain radius, this energy is high enough to unbind the pairs, locally breaking superconduc-

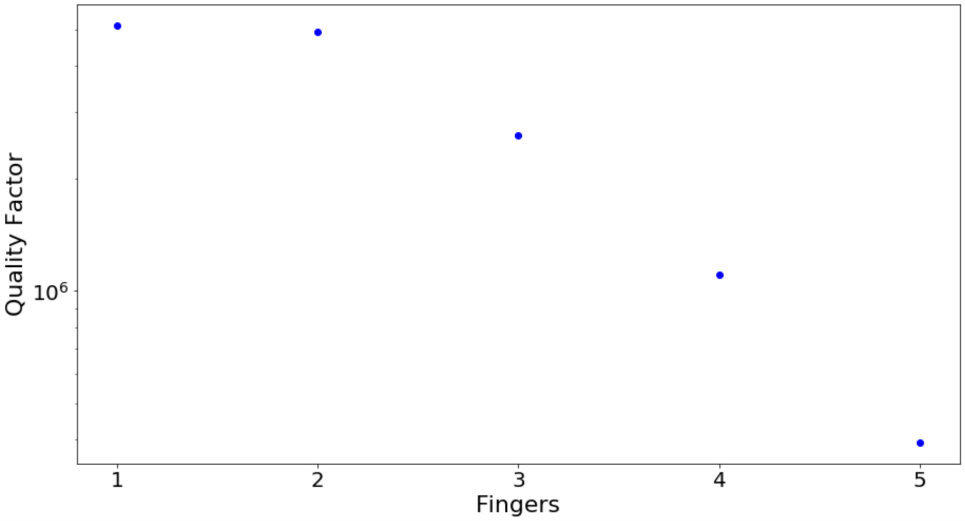

Figure 3-3: Quality Factor Plotted Against Number of Capacitive Fingers

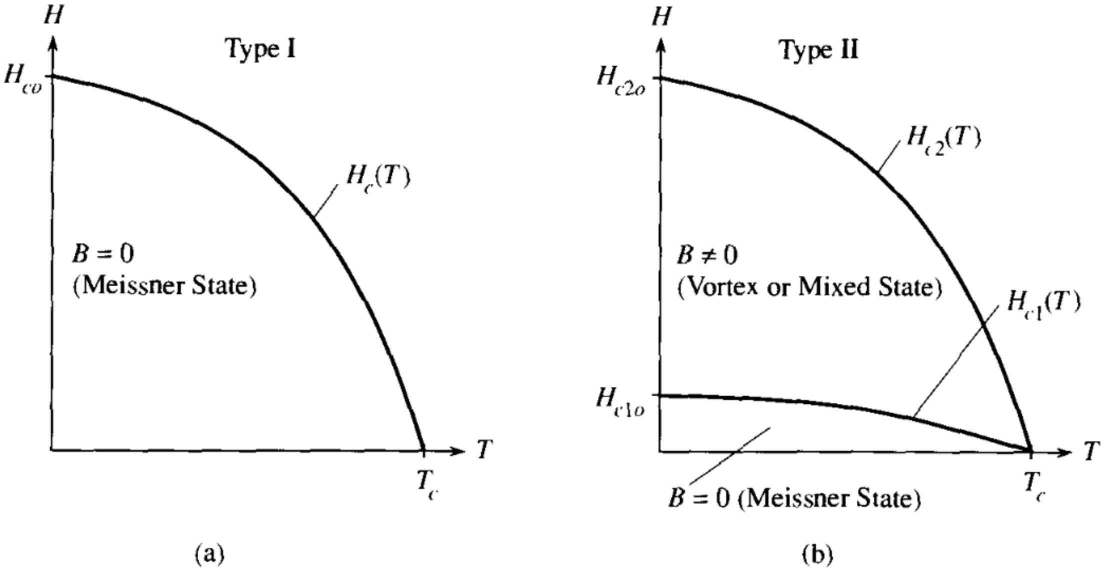
H
Type I
H_{co}
$H_c(T)$
B = 0
(Meissner State)
T
T_c
(a)
H
Type II
H_{c2o}
$H_{c2}(T)$
B ≠ 0
(Vortex or Mixed State)
$H_{c1}(T)$
H_{c1o}
T
B = 0 (Meissner State)
T_c
(b)

Figure 3-4: Phase Diagrams for Type I and Type II Superconductors. Figures reproduced from reference [20].

tivity and allowing for some resistance [20]. The loss due to vortices is proportional to this observed vortex resistance, R_v, given some current [25].

$$\frac{1}{Q_v} = \frac{R_v}{\omega L'} \tag{3.4}$$

where

$$R_v = \frac{j(x)\rho_v l}{Wd} \tag{3.5}$$

This resistance scales inversely with the width of the waveguide W and the thickness d, and is proportional to the vortex resistivity. In addition, there is a factor j(x) that takes into account the larger density of current on the edges of the center conductor [25].

$$j(x) = \frac{4}{\pi^2}\frac{W^2}{W^2 - 4x^2} \tag{3.6}$$

Using the flux per vortex, Φ_0, and the vortex density, n_v, we can bring these equations together, giving us a useful equation for vortex loss.

$$\frac{1}{Q_v} = n_v j(x)\frac{\Phi_0^2}{\omega_0 W d L'}\left(\frac{(\omega_0/\omega_p)^2 + \epsilon}{1 + (\omega_0/\omega_p)^2}\right) \tag{3.7}$$

The nature of vortices are the main cause for the critical current and fields of a type II superconductor. In a typical graph of current through NbTiN bulk film, the three phases can clearly be seen in the change of resistance (Figure 3-5).

To limit vortices, we can decrease the temperature. This phenomenon is visible in Figure 3-6, which shows the vortex-normal discontinuity at the top and the Meissner-vortex discontinuity at the bottom with varying temperatures. Though the critical current at the vortex-normal does not change with temperature, the range of the vortex state grows as temperature increases.

3.2.2 Two-Level Defects

Though vortices are an important concept to understand in the loss for type II superconductors, two-level defects on the NbTiN-air or diamond-NbTiN boundaries can contribute substantial loss at low temperatures. These are typically oxide-forms of

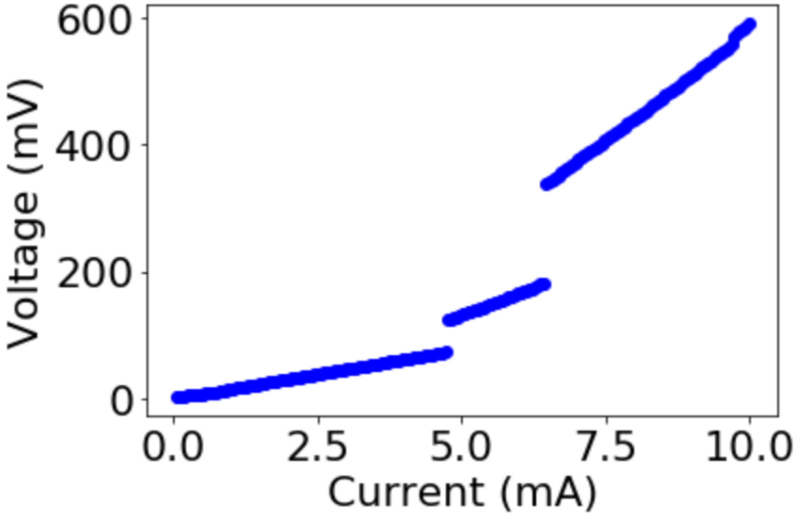

Figure 3-5: The discontinuities in this graph (collected at 2800mK) mark the increase in resistance at the boundary of each superconductor phase.

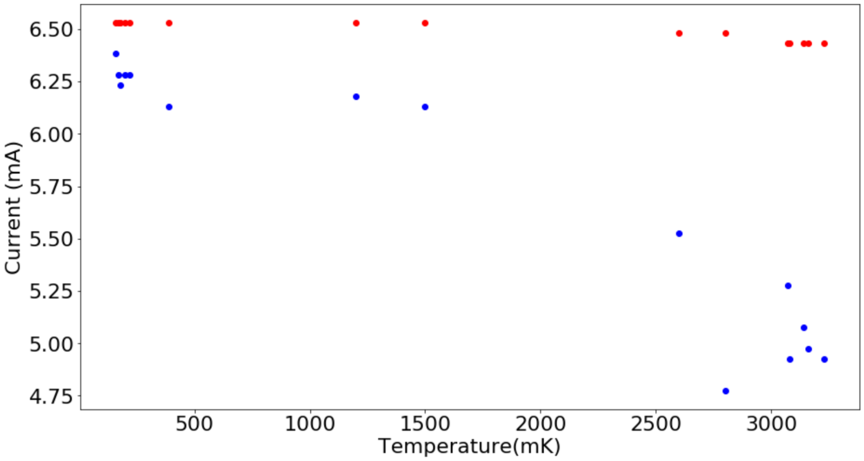

Figure 3-6: (Top) The vortex-normal critical current boundary does not change with temperature. (Bottom) The vortex Meissner-vortex discontinuity lowers with increased temperature.

the material and their existence has a strong dependence on the geometry of the resonator [25].

Because each of these defects has a different characteristic excitement energy, it is likely that some will have similar energy to that of the resonator. Further, they can couple to the CPW's fields due to their electrical dipole moments, providing a path for significant energy leakage.

Loss due to TLS is given in the following equation [25]:

$$\frac{1}{Q_{TLS}} = \frac{tanh(\hbar\omega/2k_BT)}{\sqrt{1+(E/E_s)^2}} \tag{3.8}$$

In this case, E_s represents the saturation field of the defect. As E grows, more of the defect is in the excited state and no longer contributes to loss.

Chapter 4

Procedure

4.1 Fabrication

4.1.1 Sputtering

To create NbTiN CPW resonators, we first need the ability to deposit a high-quality film of NbTiN. The deposition method used in this experiment is sputtering. (picture of sputterer)

The sputtering process used here involves ionizing Argon and then charging a plate of NbTi. The Coulombic forces cause the Argon ions to crash into the plate, launching NbTi molecules towards the substrate at an equivalent speed. Once this reaction begins, Nitrogen is added, which fills into the crystalline structure where needed.

First tests were done with NbN, a superconductor with a lower T_c but more readily available in Harvard's facilities. It is well-known that the sputtering processes for both materials are similar and that the determining factor of both is the partial pressure of nitrogen. Further, the critical temperature of both increases as the total pressure decreases, as seen in Figure 4-1, until 3 mTorr [nbtin/nbn paper]. Critical temperature is used as a measure of quality due to its correlation with critical field and its ease of measurement.

Further, the relation between Nitrogen partial pressure and critical temperature

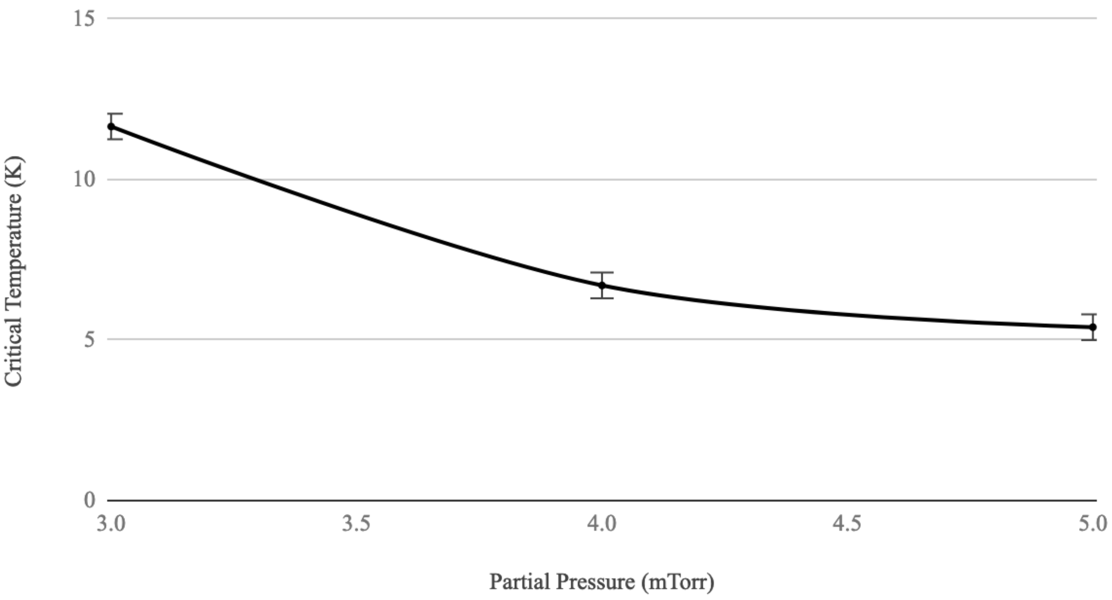

Figure 4-1: NbN critical temperature decreases as chamber pressure increases.

can be seen in the Figure 4-2 below, from [27]. The referred-to films in this figure are thinner and therefore have a lower critical temperature.

The sputtered films are approximately 100nm thick. Originally, there was also a problem such that the NbTiN films would peel off the substrate. The solution was to deposit 10nm of Titanium onto the diamond before, and then sputter NbTiN, which allows for better sticking to the dielectric.

4.1.2 Lithography Process

First attempts at lithography used an additive process for the creation of striplines. This began with spinning resist straight onto a diamond, developing and dissolving the stripline pattern, then sputtering NbTiN onto the substrate. After that, a wet etch was used to remove the excess metal and resist.

But the thickness of our CPW's was on the same order as the thickness of the resist, allowing for possible connections between unwanted and wanted film. We then replaced our resist with HSQ, whose coating thickness could be much higher. Still, a lip would be created where the NbTiN would climb the resist walls and stay after the removal step, which reduced quality of the striplines.

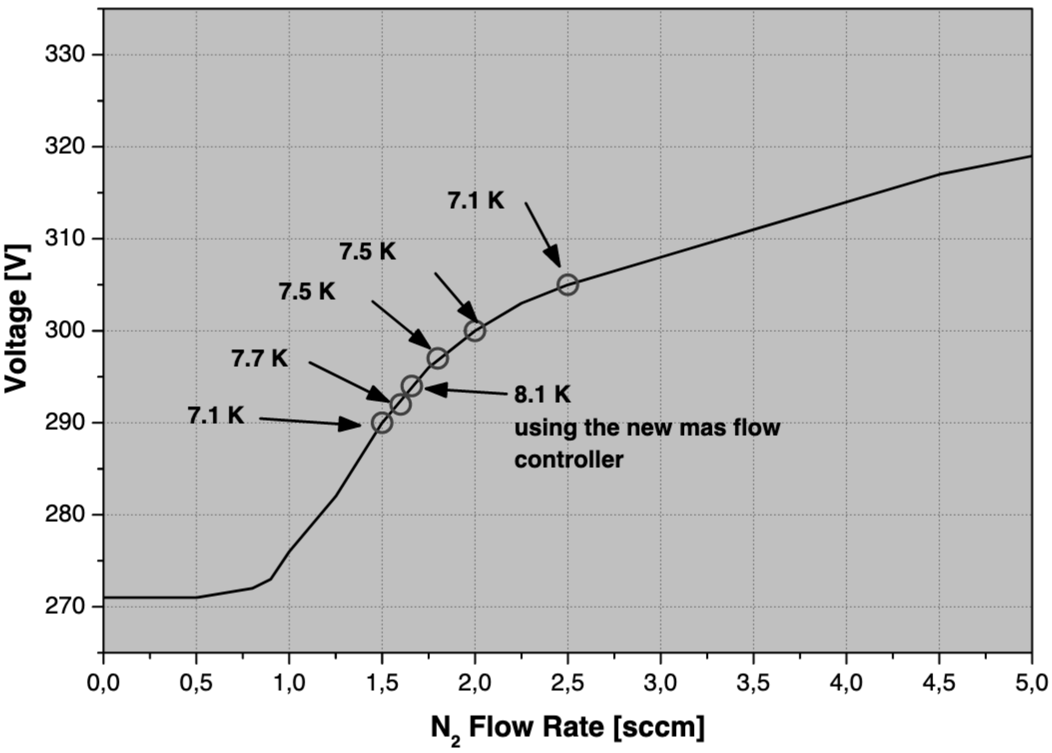

Figure 4-2: NbN critical temperature peaks at 1.66sccm Nitrogen. Figure reproduced from reference [27].

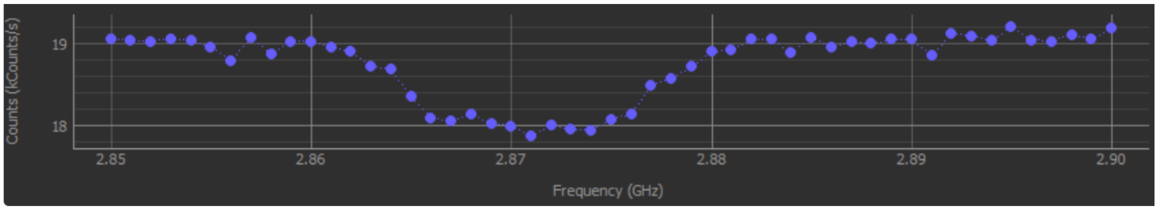

Figure 4-3: ODMR dips with NV centers

So we revamped the process, instead using a subtractive process and a dry etch. In this routine, NbTiN is deposited onto the diamond first, before spinning on and developing the resist, and etching away the exposed metal.

4.2 Experimental Setup and Measurement

4.2.1 Iterations

Our first tests were that of the setup. To test whether our cryostat would be able to allow for the measurements we needed, we first ran an ODMR experiment with gold striplines and NV centers, as both are more well-known and readily easy to use in our facilities.

Using a confocal microscope, we identified an NV center that we could couple to with our stripline. Sweeping the frequency outputted by our striplines, we find the characteristic double dip of ODMR in Figure 4-3. The dips have less amplitude than anticipated, but this is believed to be due to using a relatively unfocused confocal microscope.

We then tested our setup with superconducting striplines. At 11.6K, we were able to successfully find NV centers and measure and show superconductivity. We were unable to couple to any NV centers, though this is because we could not find any between our center conductor and ground, as seen in Figure 4-4.

4.2.2 Final Setup

Our final design can be found in Figure 4-5. The filled-in space will be etched, as we are using a negative resist.

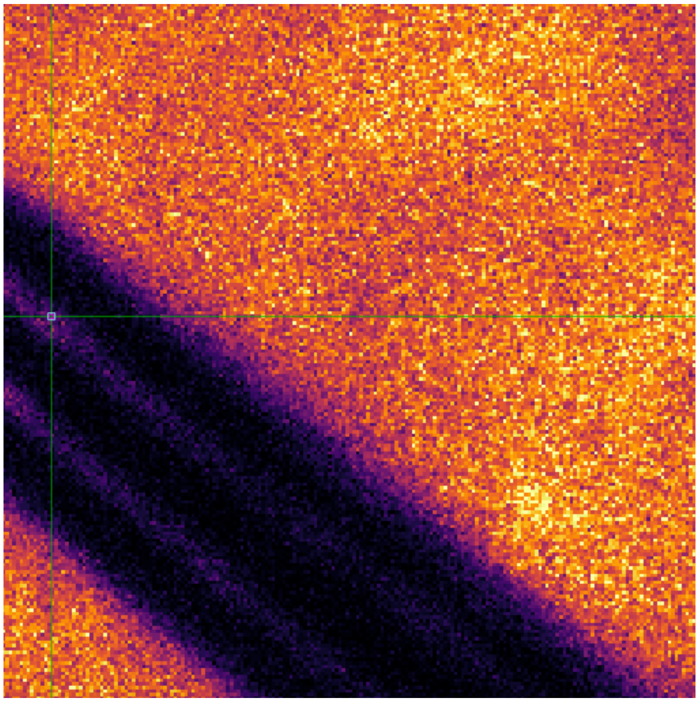

Figure 4-4: Imaging of diamond's surface using confocal microscope. The dark area is the CPW.

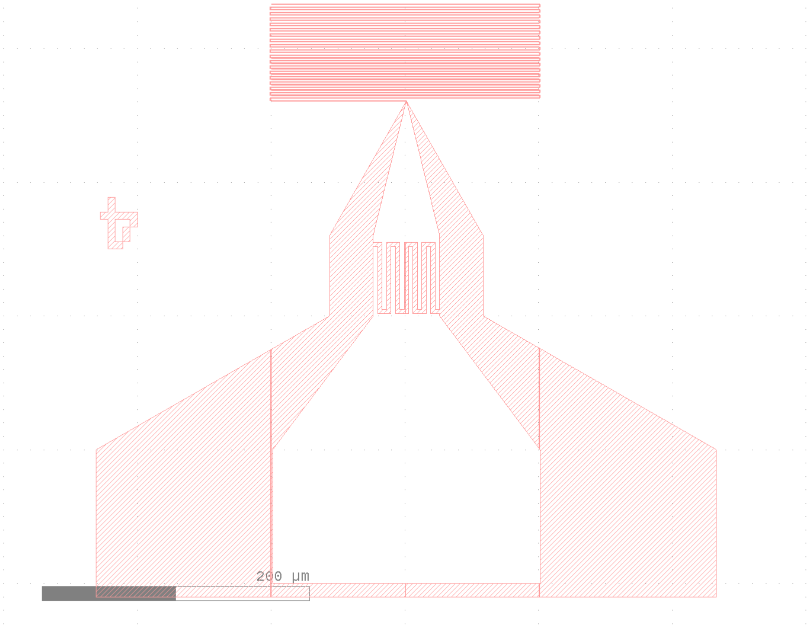

Figure 4-5: Design for 4-finger capacitively coupled CPW with 250nm-wide center conductor.

The coplanar waveguide tapers out to huge proportions for ease of wirebonding. Our goal resonance frequency is approximately 10 GHz, so we needed to keep the meanders small enough such that we could fit an approximately 7.5mm long resonator.

Gold wirebonds are then strung from these large bond-pads to a gold PCB, which connects to a coaxial cable. For frequency sweeps and continuous power measurements, this entire setup is placed in a dilution refrigerator at millikelvin temperatures. Pulsed power measurements are done in a 4K cryostat, as seen in Figure 4-6. Microwave circulators are used to separate the wire etaloning from our desired data.

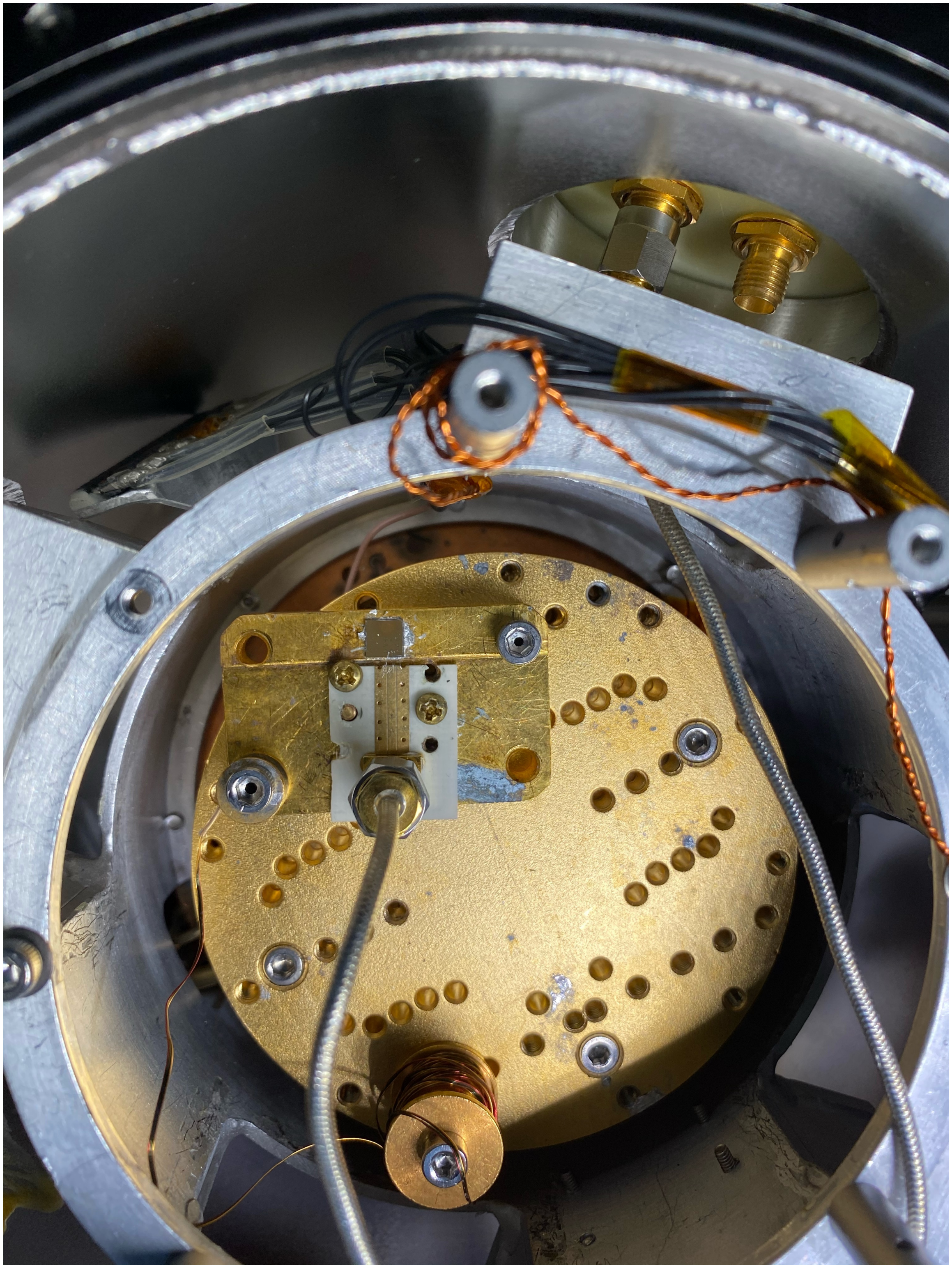

Figure 4-6: Cryostat with diamond, PCB, and stainless steel cable.

Chapter 5

Results and Conclusion

5.1 Results

5.1.1 Measured Resonance with Continuous Driving

To determine whether our CPW resonators are superconducting and resonating, we will look for the characteristic non-linearities and peaks of Niobium-based resonators. These non-linearities consist of Duffing Oscillator nonlinearities and weak link effects.

Duffing Oscillator nonlinearities form due to loss from the penetration of magnetic flux into superconductors. Due to the current's oscillation, a nonlinear inductance is introduced into the system. Duffing oscillator nonlinearities are characterized by a dramatic skewing of the resonance and a shift to lower frequencies with increased power [28].

Weak link effects, under oscillating RF currents, can cause switches between superconductive and normal states. These switches cause abrupt jumps in the reflection [29].

Together, these effects produce the scattering parameter curves from our experiment, as seen in Figure 5-1. Resonance data at different powers were shifted by an offset for clarity. Measurements were taken in a dilution refrigerator at 1150 mK, using a Vector Network Analyzer to sweep frequencies around the resonance.

At low powers, our resonance is symmetric and Gaussian. We can determine

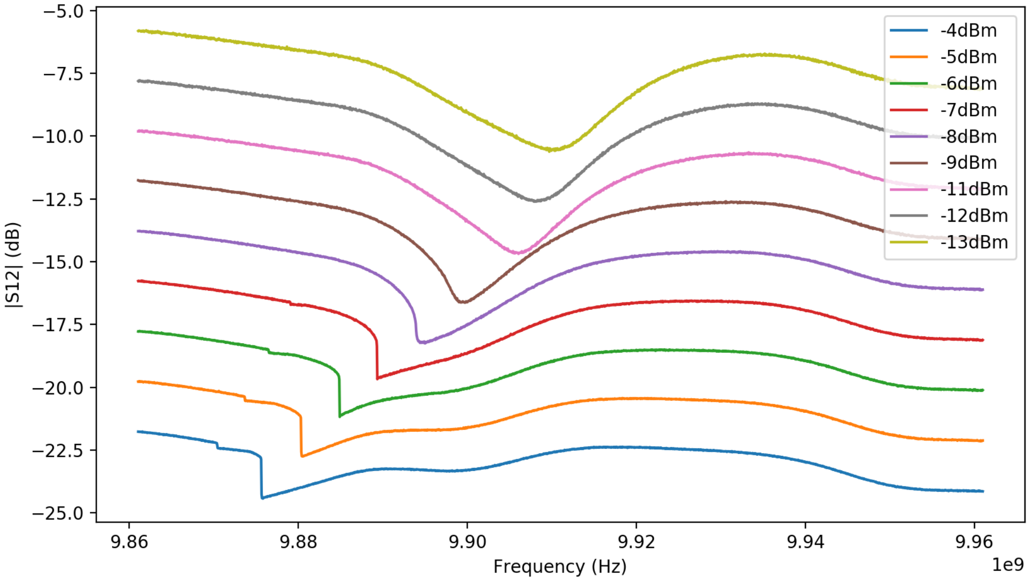

Figure 5-1: Nonlinear responses at 9.91 GHZ. As power increases, the resonance shifts, broadens, tilts, and abrupt jumps begin to appear. Resonance data at different powers were shifted by an offset for clarity.

characteristics of the quality factor and power by analyzing it in this state.

At -20 dBm, our resonance is around 9.905 GHz, pictured in Figure 5-2. The surrounding low-frequency sine wave and the smaller high-frequency oscillations are most likely due to Fabry-Perot interference from impedance mismatching at cable boundaries and temperature shifts. We can then calculate the total Q using equation 2.23, yielding a quality factor at low power of $Q = 900$.

It is possible to then subtract out the background, allowing us to get the resonance's real and imaginary S_{21} values (Figures 5-3 (a) and (b)). To find the external and internal quality factors Q_e and Q_i, we fit the complex scattering parameter to equation 5.1 [20].

$$S_{21} = 1 - \frac{Q/Q_e}{1 + 2iQ(f/f_r - 1)} \tag{5.1}$$

Fitting to this equation gives $Q_e = 35386$. Plugging back into our quality factor equation, we find $Q_i = 924$. Thus, our resonator is under-coupled (which allows us to see the intrinsic Q of our resonator better). Knowing these values allows us to find the circulating power in our resonator. This number, though, is not inherent and can

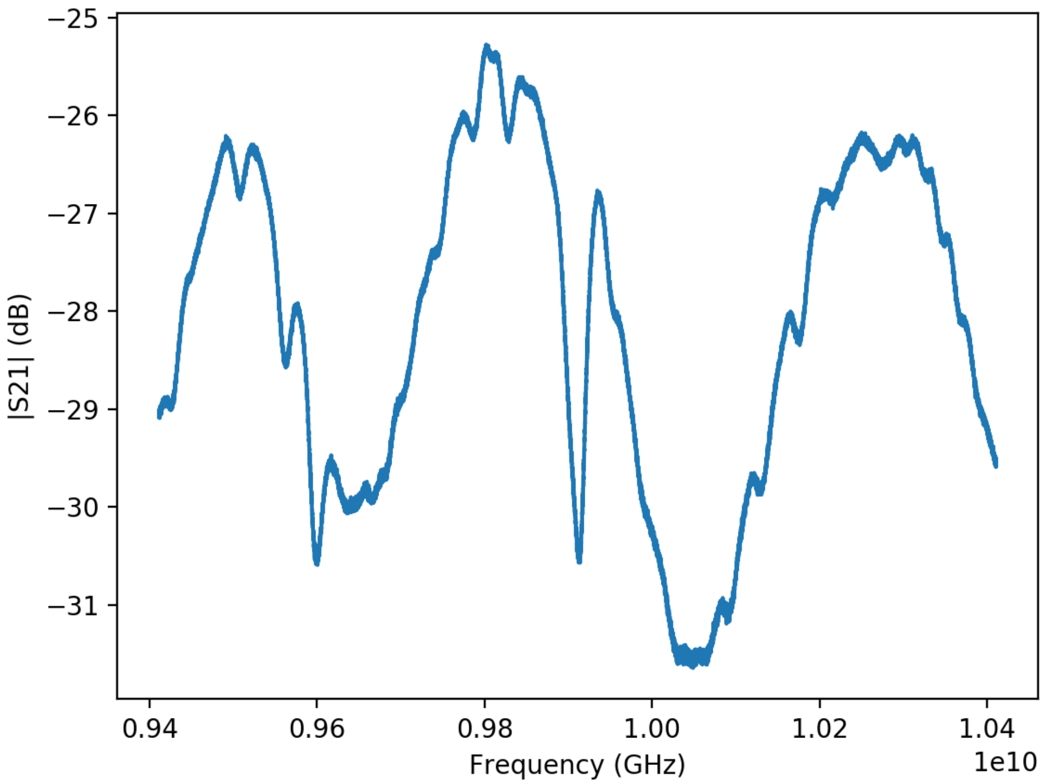

Figure 5-2: Resonator amplitude data for given frequencies.

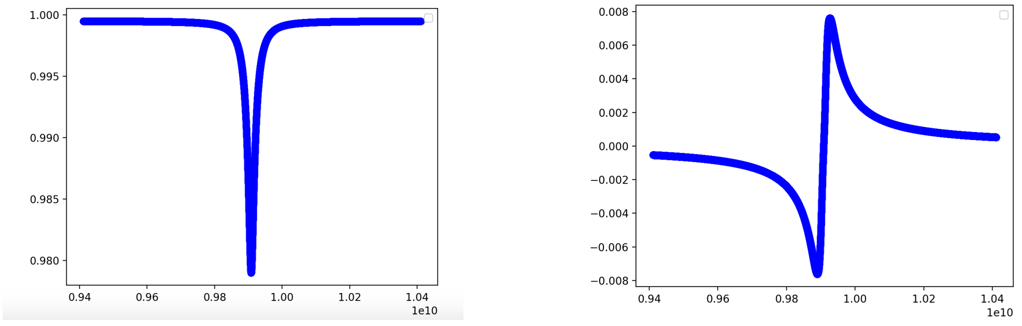

(a)

(b)

Figure 5-3: **(a)** Measured real values of S_{21} for resonance. **(b)** Measured imaginary vales of S_{21} for resonance.

be increased by increasing the coupling capacitance [30].

$$P_{circ} = \frac{P_{in}}{\pi}\frac{Q^2}{Q_e} \approx 7.7P_{in} \tag{5.2}$$

5.1.2 Pulsed Measurements

Further, as a proof of concept, we can simulate the fast pulse sequences that are done in SiV experiments, using the superconducting resonators and make sure our resonances still occur.

This entails sending O(100) ns pulses of ≈10 GHz power at a rate of O(1) kHz. This setup was created in our lab by connecting a pulse generator (30 ns pulse, 1 kHz rate) and a frequency generator (with the ability to sweep from 1 to 20 GHz) to either side of a microwave switch. The outputted signal is sent into our cryostat with our device in vacuum at 8K. Using a fast oscilloscope, we then measure the reflected power through a circulator.

Off resonance, we should see nearly the same reflectance as the power that we put in (a rectangular block of oscillations with some possible ramping down at the end). On resonance, we have a more complicated characteristic shape. Near the start of the pulse, we should see high reflectance as the resonator's circulating power builds up. The time this takes should be invariant on the pulse length. Then, the resonator's output should cancel out the reflection for the remainder of the pulse. When the power is turned off, there will be some ringing reflection from the stored power in the resonator.

Experimental demonstration of this phenomenon is found in Figure 5-4. Noise on the order of MHz was recorded but filtered out with Python post-analysis. The time invariance of the resonator's ramp-up can be seen in Figure 5-5. On resonance, we see the expected amplitude reduction of the reflected pulse as compared to off-resonance pulses. This confirms the existence of the resonance, implying the waveguide is superconducting.

After these tests, it is clear that NbTiN resonators superconduct and resonate at the temperatures used for SiV experiments. Further, they allow for the fast, long pulse sequences we desire.

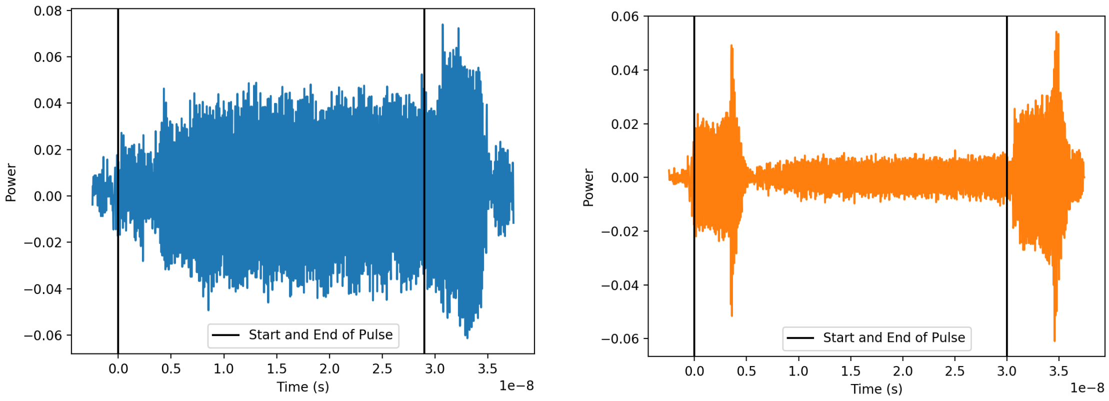

(a) (b)

Figure 5-4: **(a)** Reflected power for off-resonant frequencies. **(b)** Reflected power for resonance. Data at different pulse lengths were shifted by an offset for clarity.

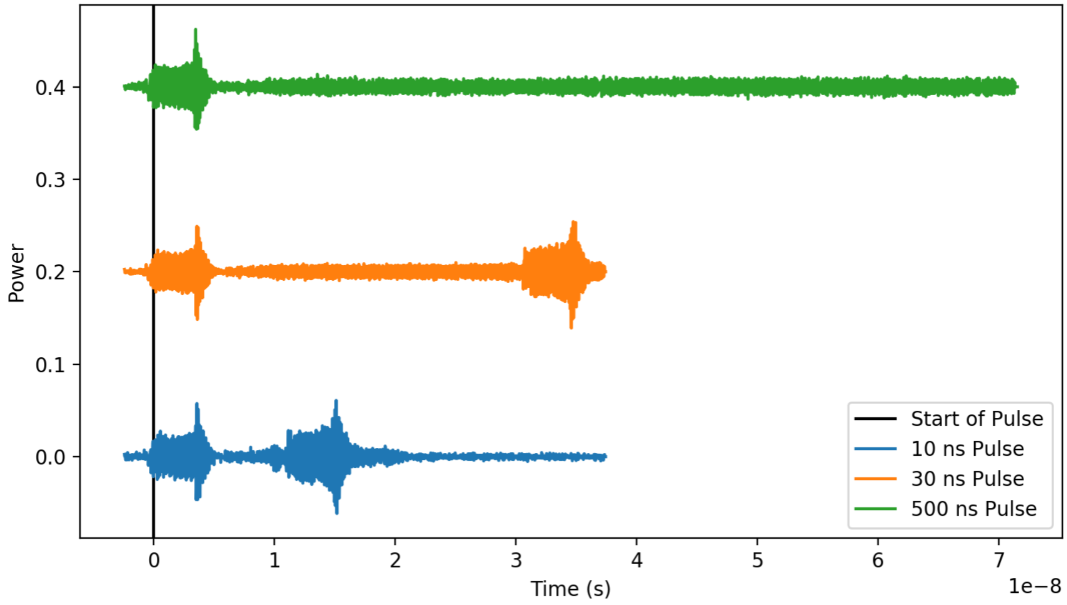

Figure 5-5: Resonator ramping will always take the same amount of time, independent of pulse length.

5.2 Conclusion and Future Work

Together, these characteristics give us the opportunity to run more efficient experiments, with a larger circuit depth, and possibly probe new, exciting areas in the field of vacancy center quantum repeaters.

One possible area that superconducting resonators can give us access to is two-qubit gates. Two-qubit gates require coupling to nearby ^{13}C nuclei through microwave driving. Due to the complicated nuclear bath and the relatively low population of ^{13}C, only very specific fields can couple. Because most of the resonance is filtered out, we require high power and high rabi frequency for even modest fidelities [16]. With superconducting striplines, our ability to drive increases, allowing for more efficient and useful two-qubit gates.

The first step in this direction requires the fabrication of superconducting striplines on a SiV-implanted diamond. Though we know the CPW resonators work, we do not know how high their effective coupling will be and how long they will allow our pulse sequences to be, as we do not have exact calibrations for the power levels required to spin-drive, and as the SiV ground state susceptibility to microwave driving varies from sample to sample. Next steps will include implementing our repeater scheme with the new CPW's, measuring fidelities, and possibly attempting entanglement purification using the ^{13}C nuclei.

Bibliography

[1] P. W. Shor, “Polynomial-time algorithms for prime factorization and discrete logarithms on a quantum computer,” *Proceedings of the 35th Annual Symposium on Foundations of Computer Science*, 1996.

[2] D. Loss and D. P. DiVincenzo, “Quantum computation with quantum dots,” *Phys. Rev. A*, 1998.

[3] J. Preskill, “Quantum computing and the entanglement frontier,” *CALT*, 2012.

[4] E. Pednault, J. Gunnels, D. Maslov, and J. Gambetta, “On “quantum supremacy”.” Blog Post by IBM Quantum.

[5] A.B.Finnila *et al.*, “Quantum annealing: A new method for minimizing multidimensional functions,” *Chemical Physics Letters*, 1994.

[6] Q. R. for Long Distance Fibre-Based Quantum Communication, “Quantum repeaters.” QuReP, 2010.

[7] C. Elliott, “Building the quantum network,” *New Journal of Physics*, 2002.

[8] C. H. Bennett and G. Brassard, “Quantum cryptography: Public key distribution and coin tossing,” *Proceedings of the International Conference on Computers*, 1984.

[9] *Corning® SMF-28® Ultra Optical Fiber Product Information.*

[10] V. R. R. Valivarthi, *Bell state measurements for quantum communication.* PhD thesis, UNIVERSITY OF CALGARY, 2017.

[11] E. Khabiboulline, “Homework 4 solutions.” Solutions to Professor Lukin’s Graduate Quantum Information Class.

[12] H. J. Briegel, *The physics of quantum information: quantum cryptography, quantum teleportation, quantum computation*, ch. 8. Springer, 2001.

[13] C. Hepp, *Electronic structure of the silicon vacancy color center in diamond.* PhD thesis, Saarland University, 2014.

[14] D. D. Sukachev *et al.*, “Silicon-vacancy spin qubit in diamond:a quantum memory exceeding 10 ms with single-shot state readout,” *Phys. Rev. Lett.*, 2017.

[15] M. K. Bhaskar *et al.*, “Experimental demonstration of memory-enhanced quantum communication,” *Nature*, 2020.

[16] C. T. Nguyen *et al.*, “An integrated nanophotonic quantum register based on silicon-vacancy spins in diamond,” *Phys. Rev. B*, 2019.

[17] R. N. Simons, *Coplanar Waveguide Circuits, Components, and Systems*, ch. 2. John Wiley and Sons, 2001.

[18] S. Gevorgian *et al.*, “Cad models for shielded multilayered cpw,” *112 IEEE TRANSACTIONS ON MICROWAVE THEORY AND TECHNIQUES*, 1995.

[19] B. C. Wadell, *Transmission Line Design Handbook.* Artech House, 1991.

[20] I. Besedin *et al.*, “Quality factor of a transmission line coupled coplanar waveguide resonator,” *EPJ Quantum Technology*, 2018.

[21] H. Hattermann *et al.*, “Coupling ultracold atoms to a superconducting coplanar waveguide resonator (supplementary material),” *Nature Communications*, 2017.

[22] J. Zhang *et al.*, “Attenuation characteristics of coplanar waveguides at subterahertz frequencies,” *IEEE TRANSACTIONS ON MICROWAVE THEORY AND TECHNIQUES*, 2005.

[23] M. Göppl *et al.*, “Coplanar waveguide resonators for circuit quantum electrodynamics,” *Journal of Applied Physics*, 2008.

[24] J. M. Sage *et al.*, “Study of loss in superconducting coplanar waveguide resonators,” *Journal of Applied Physics*, 2011.

[25] I. Nsanzineza, *Vortices and Quasiparticles in Superconducting Microwave Resonators.* PhD thesis, Syracuse University, 2016.

[26] T. Orlando and K. A. Delin, *Foundations of Applied Superconductivity*, ch. 6. Addison-Wesley, 1991.

[27] S. H. Bedorf, *Development of Ultrathin Niobium Nitridea nd Niobium Titanium Nitride Films for THz Hot-Electron Bolometers.* PhD thesis, University of Cologne, 2005.

[28] B. A. Willemsen *et al.*, “Nonlinear response of suspended high temperature superconducting thin film microwave resonators,” *IEEE TRANSACTIONS ON APPLIED SUPERCONDUCTIVITY*, 1995.

[29] B. Abdo *et al.*, “Observation of bifurcations and hysteresis in nonlinear nbn superconducting microwave resonators,” *IEEE TRANSACTIONS ON APPLIED SUPERCONDUCTIVITY*, 2006.

[30] P. Summer, “Characterization of superconducting coplanar waveguide resonators at millikelvin temperatures,” Master’s thesis, University of Munich, 2014.